

XRISM Discovery of Multiple Ionized Fe-K Emission and Absorption Components in Centaurus A

TAISHU KAYANOKI ¹, YASUSHI FUKAZAWA ¹, JUNJIE MAO ^{2,1}, JON M. MILLER ³, LUIGI GALLO ⁴,
TAHIR YAQOOB^{5,6,7}, RICHARD MUSHOTZKY ^{8,9}, DAVID BOGENSBERGER ^{10,3}, MISAKI MIZUMOTO ¹¹,
KOUICHI HAGINO ¹², HIROFUMI NODA ¹³, YOSHIHIRO UEDA¹⁴, MAKOTO TASHIRO ^{15,16}, YUYA NAKATANI ¹⁴,
TOSHIYA IWATA ¹² AND MISAKI URATA ¹

¹*Department of Physics, Graduate School of Advanced Science and Engineering, Hiroshima University, Hiroshima 739-8526, Japan*

²*Department of Astronomy, Tsinghua University, Beijing 100084, China*

³*Department of Astronomy, The University of Michigan, 1085 South University Avenue, Ann Arbor, Michigan, 48103, USA*

⁴*Saint Mary's University, Department of Astronomy and Physics, 923 Robie St, Halifax, Nova Scotia B3H 3C3, Canada*

⁵*National Aeronautics and Space Administration, Goddard Space Flight Center, Greenbelt, MD 20771, USA*

⁶*Center for Research and Exploration in Space Science and Technology, NASA/GSFC (CRESS T II), Greenbelt, MD 20771, USA*

⁷*Center for Space Science and Technology, University of Maryland, Baltimore County (UMBC), 1000 Hilltop Circle, Baltimore, MD 21250, USA*

⁸*Department of Astronomy, University of Maryland, College Park, MD 20742, USA*

⁹*Joint Space-Science Institute, University of Maryland, College Park, MD 20742, USA*

¹⁰*Université Paris-Saclay, Université Paris Cité, CEA, CNRS, AIM, 91191 Gif-sur-Yvette, France*

¹¹*Science Education Research Unit, University of Teacher Education Fukuoka, Akama-bunkyo-machi, Munakata, Fukuoka 811-4192, Japan*

¹²*Department of Physics, The University of Tokyo, 7-3-1 Hongo, Bunkyo-ku, Tokyo 113-0033, Japan*

¹³*Astronomical Institute, Tohoku University, 6-3 Aramaki-zaaoba, Aoba-ku, Sendai, Miyagi 980-8578, Japan*

¹⁴*Department of Astronomy, Kyoto University, Kitashirakawa-Oiwake-cho, Sakyo-ku, Kyoto 606-8502, Japan*

¹⁵*Department of Physics, Saitama University, Saitama 338-8570, Japan*

¹⁶*Institute of Space and Astronautical Science (ISAS), Japan Aerospace Exploration Agency (JAXA), Kanagawa 252-5210, Japan*

ABSTRACT

We present the first clear detection of ionized Fe-K emission and absorption components in the nearby radio galaxy Centaurus A, revealed by the high-resolution XRISM/Resolve detector. In the 6.5–6.9 keV band, XRISM reveals multiple Fe XXV and Fe XXVI emission components. One is a broad (with a width of $\sigma = 3000$ km/s) and redshifted (+3400 km/s) component, originating at $D = 0.02$ pc from the central black hole. The other two components are narrow (with a width of $\sigma = 500$ km/s) and exhibit redshifted and blueshifted velocities (+2600 km/s and -1500 km/s), originating from more distant regions ($D = 0.1$ pc). The photo-ionized model explains the broader component, while the two narrower components can be explained by either photo-ionization or collisional ionization. One interpretation is that the broader component is an outflow at $\sim 10^2 R_S$ (R_S ; Schwarzschild radius) and the narrow component is a shock-heated plasma close to the torus, with a possible connection to the JWST-discovered outflow outside the torus. Two blueshifted absorption lines are detected at ~ 7.1 keV ($\sim 10^4$ km/s) and ~ 10.6 keV ($\sim 10^5$ km/s). The line significance of the 10.6 keV line is above 98%. The absorption line components might be attributed to the broad emission component. These results demonstrate the high potential of XRISM/Resolve to characterize ionized emission and absorption features in the Fe-K band. Our findings establish a new benchmark in the study of circumnuclear environments in low-luminosity radio galaxies, thereby contributing to a broader understanding of AGN unification.

Keywords: Active galactic nuclei (16) — X-ray active galactic nuclei (2035) — Black holes (162)

1. INTRODUCTION

Active Galactic Nuclei (AGN) emit radiation across a wide wavelength range, from radio to gamma-rays.

In non-beamed AGNs, the X-ray emission is primarily a power-law component from the hot corona close to the central supermassive black hole, and it is often absorbed by the dust torus in the case of type-2 AGNs. Additionally, a reflection component from the cold dust torus is associated with the neutral Fe-K emission line (e.g., K. A. Pounds et al. 1989; H. Awaki et al. 1991; T. Yaqoob & U. Padmanabhan 2004; X. W. Shu et al. 2010; Y. Fukazawa et al. 2011). Moreover, ionized emission lines in the Fe-K band have been detected in several AGNs, such as NGC 7314 (T. Yaqoob et al. 2003), M81 (M. J. Page et al. 2004), Mrk 590 (A. L. Longinotti et al. 2007), IRAS 18325–5926 (A. P. Lobban & S. Vaughan 2014), etc. However, due to the poor energy resolution in the CCD spectra and the smaller effective area of grating spectra, it has been difficult to detect ionized emission lines in the Fe-K band of AGNs. Thus, it remains difficult to determine whether such ionized emission lines truly exist, whether they are a common feature of AGNs, and to distinguish whether the ionization mechanism is photo-ionization or collisional ionization.

AGNs accrete mass onto supermassive black holes (SMBHs) and often exhibit outflows as relativistic jets or ionized winds. Ionized winds are characterized and classified by their ionization parameter ξ , hydrogen column density N_{H} , and outflow velocity. The ionization parameter is defined as

$$\xi = \frac{L_{\text{ion}}}{n_{\text{H}} r^2} \quad (1)$$

where L_{ion} (1 – 1000 Ryd, 1 Ryd = 13.6 eV) denotes the ionizing source luminosity, n_{H} represents the hydrogen number density of the disk wind, and r indicates the distance from the source (C. B. Tarter et al. 1969; L. C. Gallo et al. 2023). Ultrafast outflows (UFOs, F. Tombesi et al. 2010) with velocities faster than 10^4 km s⁻¹ can be very energetic (Xrism Collaboration et al. 2025) and are highly ionized with ionization parameters $\log \xi$ (erg cm s⁻¹) = 2 – 7 and high column densities of $\log N_{\text{H}}$ (cm⁻²) = 22 – 25 (S. Laha et al. 2021; S. Yamada et al. 2024). They are generally observed as blueshifted absorption lines at 7 – 10 keV (F. Tombesi et al. 2010). Based on the CCD data prior to XRISM, their occurrence rate is estimated to be $\sim 40\%$ of X-ray bright AGN (F. Tombesi et al. 2010, 2011; J. Gofford et al. 2013), but is poorly determined.

AGNs are classified as either radio-loud or radio-quiet based on their radio intensity. The spectral energy distributions (SEDs) of radio-loud and radio-quiet AGNs are broadly similar across the infrared to X-ray bands; however, their radio and gamma-ray luminosities differ owing to the strong relativistic jets present in the radio-loud AGNs (e.g. C. M. Urry & P. Padovani 1995;

T. Kayanoki & Y. Fukazawa 2022). In principle, radio galaxies are radio-loud AGNs with jets misaligned from the line of sight, which allows for the observation of emissions from both the jets and the central core in such galaxies. Therefore, radio galaxies are ideal objects for investigating the relationship between the jet and the accretion disk. Recently, several groups have conducted sample studies on radio galaxies, focusing on topics such as UFOs (e.g., F. Tombesi et al. 2014), X-ray neutral absorption (T. Kayanoki & Y. Fukazawa 2022), and GeV gamma-ray emission (Y. Fukazawa et al. 2016, 2022; H. Mataka & Y. Fukazawa 2023).

Centaurus A (Cen A), the nearest radio galaxy at a distance of 3.8 ± 0.1 Mpc (G. L. H. Harris et al. 2010), has an optical spectrum dominated by narrow lines, so it is classified as a type-2 AGN (V. Beckmann et al. 2011) or LINER with a black hole mass of $(5.5 \pm 0.3) \times 10^7 M_{\odot}$ (N. Neumayer et al. 2007; M. Cappellari et al. 2009; M. J. Koss et al. 2022). The Schwarzschild radius is $R_{\text{S}} = 2GM_{\text{BH}}/c^2 = 1.63 \times 10^{13}$ cm. Based on its radio lobe morphology, Cen A is classified as a Fanaroff–Riley type I galaxy (B. L. Fanaroff & J. M. Riley 1974). In the soft X-ray band, an emission line component is present from the hot plasma of its host galaxy (e.g., F. Tombesi et al. 2014; Y. Fukazawa et al. 2016, Urata et al. in prep.). F. Tombesi et al. (2014) analyzed the *Suzaku* and *XMM-Newton* CCD spectra deeply and detected an absorption line in the Fe-K band. This feature is most likely Fe XXV, and the best-fit parameters of an ionized absorption model yielded $\log \xi \sim 4.3$ erg cm s⁻¹, $N_{\text{H}} \sim 4 \times 10^{22}$ cm⁻², and $v_{\text{out}} < 0.005c$. A. Alonso-Herrero et al. (2025) reported results from JWST/MIRI observations of the Cen A core, identifying an ionized flowing component. This component consists of a narrow ($\sigma \sim 600$ km s⁻¹) and fast (reaching approximately +1000, –1400 km s⁻¹) flow in the inner 6 pc region. However, no significant ionized emission component in the Fe-K band had been previously detected in past grating spectra (D. Bogensberger et al. 2024).

The first XRISM paper on Cen A (D. Bogensberger et al. 2025) focused on an analysis of the neutral Fe K α fluorescence line. In this paper, we focus on the ionized emission line and the absorption line features using broadband XRISM/Resolve data and simultaneous NuSTAR spectra obtained almost simultaneously.

2. OBSERVATION AND DATA REDUCTION

Cen A was observed by XRISM (M. Tashiro et al. 2025) in August 2024 (Table 1) with simultaneous observations by *NuSTAR* and *Chandra* (Table 1). In this analysis, we used the XRISM/Resolve (Y. Ishisaki et al. 2025; R. L. Kelley et al. 2025) data for the line study

and the *NuSTAR* spectrum (F. A. Harrison et al. 2013) to determine the hard X-ray continuum.

2.1. XRISM

The data reduction for XRISM/Resolve is the same as that described in D. Bogensberger et al. (2025). The data from the XRISM pipeline were reprocessed using the XRISM software in HEASoft release version 6.34 and the XRISM CalDB version 9 of the XRISM calibration database. The large matrices were used for the spectral response matrices (RMFs). The ancillary response file (ARF) was created for a single attitude bin, as described in the Quick-Start Guide, version 2.1.

The flux level of Cen A in the XRISM/Resolve spectrum is at least 20 times higher than that of the estimated NXB background. Therefore, we did not subtract the background spectrum, similar to the analysis of NGC 4151 (XRISM Collaboration et al. 2024). X-ray emission from Cen A is somewhat contaminated by X-ray radiation from the jet, X-ray binaries, and diffuse X-ray emission, which are not resolved by XRISM. From the *Chandra* simultaneous observations, the flux of the X-ray binaries and jet in Cen A is estimated to be less than 10% of the Resolve spectrum, and thus their contribution was ignored in our analysis.

2.2. NuSTAR

The *NuSTAR* data were reprocessed using the CalDB updated on September 30, 2024, which is applicable to the Cen A observation period. In the *NuSTAR* observation, there was a solar flare; therefore, the time intervals with background count rates $> 3\sigma$ were filtered out with the Chandra Interactive Analysis of Observations (CIAO, A. Fruscione et al. 2006) version 4.16 `lc_sigma_clip` task. The flux level and photon index of the FPMA and FPMB spectra for each observation ID were consistent within a 1σ error. We then combined the two observations using the HEASOFT (ver. 6.34) `addspec` tool. However, we did not combine the FPMA and FPMB spectra. The flux level and photon index of the combined spectra were also consistent with those of the non-combined spectra. To correct for cross-calibration between the XRISM/Resolve and NuSTAR spectra, the FPMA and FPMB spectra were rescaled by a factor of 1.08, based on the flux level in the 11–12 keV energy range (Fig. 1).

3. SPECTRAL ANALYSIS

We performed the spectral analysis using the SPEX code v3.08.01 (J. S. Kaastra et al. 2024). For the spectral analysis, the XRISM/Resolve spectra were used in

the energy range of 3.0–12.0 keV, and the `obin` command of the SPEX code was applied to perform optimal binning, following J. S. Kaastra & J. A. M. Bleeker (2016). The two NuSTAR spectra (FPMA & FPMB) were utilized for the 11.2–60.0 keV range, and we also applied the optimal binning. The spectral fitting was performed on the XRISM/Resolve and NuSTAR spectra using the *C*-statistic (J. S. Kaastra 2017). To evaluate the fitting results, we used the corrected Akaike information criterion (AICs, H. Akaike 1974; N. Sugiura 1978; A. R. Liddle 2007). Following M. Z. Buhariwalla et al. (2024), we consider ΔAIC values better than 6 to indicate that one model is significantly preferred over another at the 95% confidence level (M. Y. J. Tan & R. Biswas 2012). In all fitting models, two neutral absorption models (`hot` model in SPEX) were multiplied to account for the absorption by our Galaxy and the host galaxy of Cen A. The column density for our Galaxy was fixed to $N_{\text{H}} = 2.36 \times 10^{20} \text{ cm}^{-2}$ (HI4PI Collaboration et al. 2016), while that of the Cen A host galaxy was fitted as a free parameter at the cosmological redshift. For reflection, absorption, and emission models, we consider the protosolar abundances of K. Lodders et al. (2009). For the redshift, we adopt $z = 0.001877$ (M. J. Koss et al. 2022) for the spectral fitting. The errors for each parameter represent the 1σ confidence level.

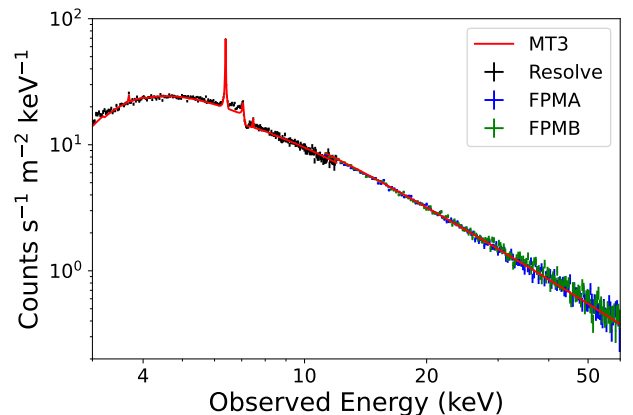


Figure 1. XRISM/Resolve (3–12 keV) and NuSTAR (11.2–60 keV) spectra with the model curve of the MT3 model, wherein the black point, the blue point, the green point, and the red line represent the Resolve spectra, FPMA spectra, FPMB spectra, and the model curve of the MT3 model, respectively. The Resolve spectrum is binned by a factor of 10 after the optimal binning for visual clarity.

3.1. Continuum modeling

Before analyzing the lines, we performed continuum modeling of the 3–60 keV X-ray spectra (Fig. 1). First,

Table 1. Cen A observations

Satellite	Obs.ID	Observation start (UT)	Observation end (UT)	Net Exp (ksec)
<i>XRISM</i>	300019010	2024/08/04 09:17:04	2024/08/09 16:24:04	225.1
<i>NuSTAR</i>	60901034002	2024/08/05 07:01:09	2024/08/05 19:26:09	22.1
<i>NuSTAR</i>	60901034004	2024/08/09 02:16:09	2024/08/09 19:21:09	72.4
<i>Chandra</i>	29490	2024/08/07 06:51:52	2024/08/07 13:21:36	20.4

we fitted the spectra with an absorbed power law. We refer to this model as the Absorbed Power-law model (AP model), which is defined as

$$\text{hot} \times \text{red} \times (\text{hot} \times \text{etau} \times \text{pow}) \quad (2)$$

where `reds` is the redshift model. The cut-off energy for the power-law component was fixed at 370 keV (C. Ricci et al. 2018) using the `etau` model in SPEX. Our results are independent of the cut-off energy. The photon index becomes $\Gamma = 1.926 \pm 0.004$, and the hydrogen column density in the host galaxy becomes $N_{\text{H}} = (1.68 \pm 0.01) \times 10^{23} \text{ cm}^{-2}$. This model provides a good fit to the continuum well in this energy band. Hereafter, we used this model as a baseline continuum model.

3.2. Search for lines

Based on the AP model, we performed the line search using a sliding Gaussian technique. The Gaussian FWHM was fixed at 8 eV, roughly twice the Resolve resolution, and this search is optimized for features with $\sim 400 \text{ km s}^{-1}$ width at 6 keV. The line center energy was varied from 3.5 to 12.0 keV in steps of 4 eV. Fig. 2 shows the significance of the line against the search energy. Line candidates above the 4σ confidence level were again fitted by letting the FWHM and line energy vary freely. The results are summarized in Table 2. When the narrow emission lines could not be fit due to the presence of broadened emission line components, the FWHM was fixed at 30 eV. Significance levels at 4 – 6 keV may not be properly evaluated due to residuals (Fig. 2a). The cause of the residuals is that the AP model was used, and the Fe-K emission lines are not explained. However, since this energy band is not the focus of this paper, it does not affect the results and discussion of the ionization component. As a result, seven emission lines and three absorption lines were found in the Resolve spectrum above the 4σ confidence level. Two additional cases with a step of 1 eV and a Gaussian FWHM of 2 eV or a step of 2 eV and a Gaussian FWHM of 4 eV were also investigated, and it was confirmed that these two cases gave the same result as the case of a step of 4 eV and a Gaussian FWHM of 8 eV.

Considering that the number of trials is $((12.0 - 3.5)/0.004 = 2125)$, the line significance would still be over 90%, for all lines in the table. For example, in this trial, the significance of the 10.6 keV absorption line is 4.61σ (99.99980%). Therefore, the post-trial significance is considered to be $1 - (1 - 0.9999980031) \times 2125 = 0.9957565$ (2.63σ). In addition, to evaluate the significance of the 10.6 keV absorption line feature, we ran Monte Carlo simulations using the `simulate` command in the SPEX code to quantify the incidence of fake lines when sliding a Gaussian between 7.5 and 12.0 keV. We simulated 1,000 times using the same net exposure time. To check the probability of detecting a Gaussian absorption trough due to random fluctuations in the simulated data, we simulated with the power-law model and performed the line search by adding a Gaussian function and sliding it. The Gaussian FWHM was fixed at 8 eV, and the line center energy was changed with a step of 4 eV increments from 7.5 to 12.0 keV. The number of the absorption lines above the 4σ confidence level was 104 in the 1,000 simulations. The absorption line candidates above the 4σ confidence level were again fitted by letting the FWHM and line energy vary freely. Then, the number of absorption lines above the 4σ confidence level was 41 in the 1,000 simulations. However, 23 of the 41 lines only covered 1-2 bins, and the obtained FWHM was almost 0 eV. From Table 2, the FWHM of the observed lines is over 10 eV. Thus, after excluding the 23 lines with 0 eV FWHM, we found that $18/1000 \sim 1.8\%$ of the simulated spectra produce spurious lines.

Most of the lines in the line search are considered Fe-K lines, but the fluorescent Ca-K line, Ni-K line, and a 5.15 keV absorption line are also present. The latter might be a blueshifted Ca-K line. Its velocity is similar to that of the ionized Fe-K emission lines. These weak ionized emission and absorption lines would not be resolved with CCD resolution, because they would be buried in the tail of the strong neutral Fe-K α line. In this paper, we focus on the ionized Fe-K emission and absorption lines. The neutral Ca-K and Ni-K will be treated in a future paper.

Table 2. Lines above the 4σ confidence level

$E_{\text{obs}}^{\text{a}}$ (keV)	ID	$E_{\text{rest}}^{\text{b}}$ (keV)	σ^{c}	FWHM (eV)	$v_{\text{shift}}^{\text{d}}$ (km/s)	Emit/Abs ^e
3.6885 ± 0.0007	Ca $K\alpha$	3.6917	5.8	6 ± 2	260 ± 60	E
5.151 ± 0.003	Ca xx	5.129	4.3	22_{-6}^{+12}	-1300 ± 200	A
$6.3989_{-0.0003}^{+0.0002}$	Fe $K\alpha$	6.4038	59.7	29.7 ± 0.7	220 ± 10	E
$6.644_{-0.004}^{+0.003}$	Fe xxv	6.700	5.9	30 (fix)	2500_{-200}^{+100}	E
6.733 ± 0.003	Fe xxv	6.700	5.2	30_{-6}^{+7}	-1400 ± 100	E
7.000 ± 0.003	Fe xxvi	6.973	7.2	30 (fix)	-1100 ± 100	E
$7.054_{-0.002}^{+0.001}$	Fe $K\beta$	7.058	12.7	30 (fix)	170_{-80}^{+40}	E
7.111 ± 0.001	Fe xxv	6.700	4.4	9_{-3}^{+4}	-12810 ± 40	A
7.478 ± 0.002	Ni $K\alpha$	7.478	5.8	21_{-4}^{+5}	0 ± 80	E
10.618 ± 0.002	Fe xxv	6.700	5.5	16 ± 5	-129120 ± 50	A

a: Observed line center energy in Cen A frame. b: Theoretical Energy (rest-frame). The line identifications are derived from the AtomDB database 3.1.3 (A. Foster et al. 2025). c: Significance level of the line. d: velocity shift. e: "E" means an emission line, and "A" means an absorption line.

3.3. Physical modeling for the neutral fluorescence lines

As a next step, we modeled the neutral fluorescence lines. Following D. Bogensberger et al. (2025), these lines were modeled with the MyTorus model (K. D. Murphy & T. Yaqoob 2009). The model file is `myt1_V000HLZnEp000_v01.fits` file (T. Yaqoob 2024) was used as the MyTorus model. For modeling the line broadening due to Doppler and relativistic effects, the `spei` model (R. Speith et al. 1995) was applied to the MyTorus model, corresponding to the `rdblur` model in XSPEC as used in D. Bogensberger et al. (2025). The photon index and normalization of the MyTorus model were linked to the power law (`pow`) model. The inclination angle, inner radius, and outer radius of the `spei` model were fixed to those of Model C in D. Bogensberger et al. (2025) to save computing time. As the Model C in D. Bogensberger et al. (2025), three MyTorus models were used to represent the neutral Fe-K lines. In our fitting, the free parameters were the three column densities of MyTorus. Because the Ni- $K\alpha$ and the Ca- $K\alpha$ lines are not included in the MyTorus model, the Gaussian models were added to express them. In summary, the model to fit the neutral fluorescence lines is

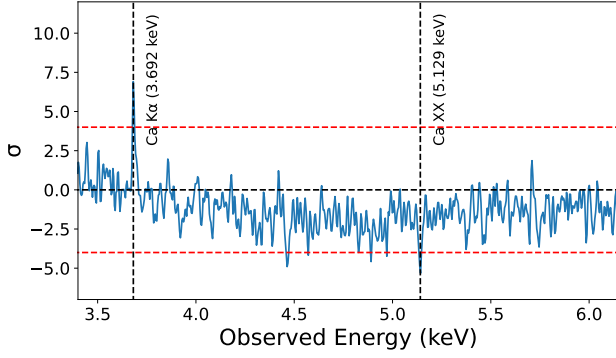
$$\text{hot} \times \text{reds} \times \left\{ \text{hot} \times \text{pow} + \sum_{i=1}^2 \text{gaus}_i + \sum_{i=1}^3 (\text{MyTorus}_i \times \text{pow} \times \text{spei}_i) \right\} \quad (3)$$

Hereafter, we refer to this model as the MT3 model. Fig. 1 shows the fitting result around the neutral Fe-K lines, and Table 3 summarizes the best-fit parameters.

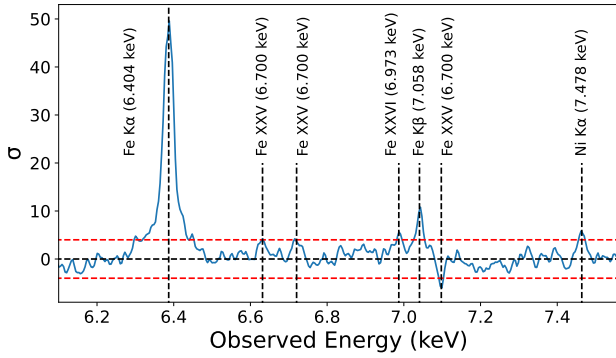
Parameter values are almost consistent with those of D. Bogensberger et al. (2025). The small difference is attributed to the different energy band used for fitting. Looking at Fig. 3, the neutral Fe-K line profiles are well represented. However, significant residuals are seen between the Fe- $K\alpha$ and Fe- $K\beta$ lines, and they are not explained by a single or a few narrow lines. Such a residual was also reported in D. Bogensberger et al. (2025), suggesting the existence of ionized Fe-K emission lines.

3.4. Gaussian modeling for ionized Fe-K emission lines

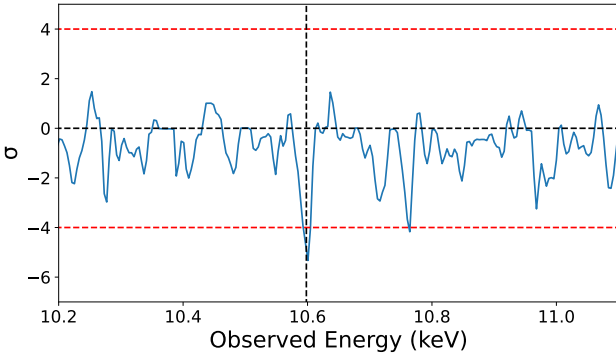
As Fig. 3 shows, the measured spectrum exceeds the best-fit MT3 between 6.5-7.0 keV. First, we tried to use Gaussian models to represent this excess. Table 2 suggested that at least three Gaussian model components are needed. Then we introduced three Gaussian model components and thawed the FWHM, line energy, and normalization parameters of the Gaussian model. Their FWHM were ~ 70 eV (for redshifted Fe xxv), ~ 30 eV (for blueshifted Fe xxv), and ~ 70 eV (for redshifted Fe xxvi). The Gaussian model component for blueshifted Fe xxv was consistent with the result in Table 2. However, even with this model, narrow line features still remained at 6.64 keV and 6.98 keV. Therefore, we added two more Gaussian model components (a total of five for the 6.5 – 7.0 keV excess) to represent these features (Fig. 3). These lines are likely a redshifted Fe xxv line and a blueshifted Fe xxvi line. As a result, three ionized components were required to represent the excess at 6.5 – 7.0 keV.



(a) 3.4 – 6.1 keV band



(b) 6.1 – 7.5 keV band



(c) 10.2 – 11.1 keV band

Figure 2. Results of sliding Gaussian for line search. The step is 4 eV, and the Gaussian FWHM was fixed at 8 eV. Horizontal red dashed lines represent the 4σ confidence level.

3.5. Physical modeling of the ionized emission line features

In this subsection, we will fit the Fe-K band excess using physical models. We applied for the photo-ionization (PIE) model (**pion** model, L. Di Gesu et al. 2017; J. Mao

Table 3. Best-fit parameters of the MT3 model.

Parameter	Unit	MT3 model
pow Γ ⁽¹⁾		1.876 ± 0.004
pow Norm ⁽²⁾		6.80 ± 0.07
hot N_{H} ⁽³⁾	10^{23} cm^{-2}	1.56 ± 0.01
MyTorus N_{H} ⁽⁴⁾	10^{23} cm^{-2}	$1.12^{+0.08}_{-0.07}$
spei R_{in} ⁽⁶⁾	r_{g}	7.2×10^5 (fixed)
spei R_{out} ⁽⁷⁾	r_{g}	7.9×10^5 (fixed)
spei i ⁽⁸⁾	deg	30 (fixed)
spei q ⁽⁹⁾		2.2 (fixed)
MyTorus N_{H} ⁽⁴⁾	10^{23} cm^{-2}	0.44 ± 0.08
spei R_{in} ⁽⁶⁾	r_{g}	5.7×10^4 (fixed)
spei R_{out} ⁽⁷⁾	r_{g}	6.3×10^4 (fixed)
MyTorus N_{H} ⁽⁴⁾	10^{23} cm^{-2}	1.6 ± 0.1
spei R_{in} ⁽⁶⁾	r_{g}	1.0×10^3 (fixed)
spei R_{out} ⁽⁷⁾	r_{g}	3.3×10^4 (fixed)
C -stat / d.o.f.		4033.8 / 3360
AICs		4058.0

- (1) Photon index of the power-law component. (2) Normalization of the power-law component in $10^{50} \text{ ph s}^{-1} \text{ keV}^{-1}$ at 1 keV. (3) Column density of neutral ISM gas in the host galaxy of the AGN. (4) Column density of the reflector. (5) Normalization of the MyTorus in $10^{50} \text{ photons s}^{-1} \text{ keV}^{-1}$ at 1 keV. This value is coupled to the normalization of the X-ray power-law component. (6) Inner radius of the reflector. (7) Outer radius of the reflector. (8) Inclination angle of the reflector (angle between the line of sight and the rotation axis of the reflector). (9) Index of radial emissivity power-law profile of the reflector.

et al. 2018) and the collisional ionization (CIE) model (**cie** model, J. S. Kaastra et al. 1996).

3.5.1. Photo-ionized emission modeling

The **pion** model calculates the transmission and emission of a slab of photo-ionized plasma based on the spectrum of the ionizing source, which can be estimated from the broadband fitting along with detailed emission and absorption features (J. Mao et al. 2019). The free parameters were a hydrogen column density N_{H} (cm^{-2}), ionization parameter $\log \xi$ (erg cm s^{-1}), and outflow velocity v_{out} (km s^{-1}). Here, the observed Cen A power-law component without any absorption was assumed as the spectrum of the ionizing source. In addition, there are two covering factors in the **pion** model. The covering

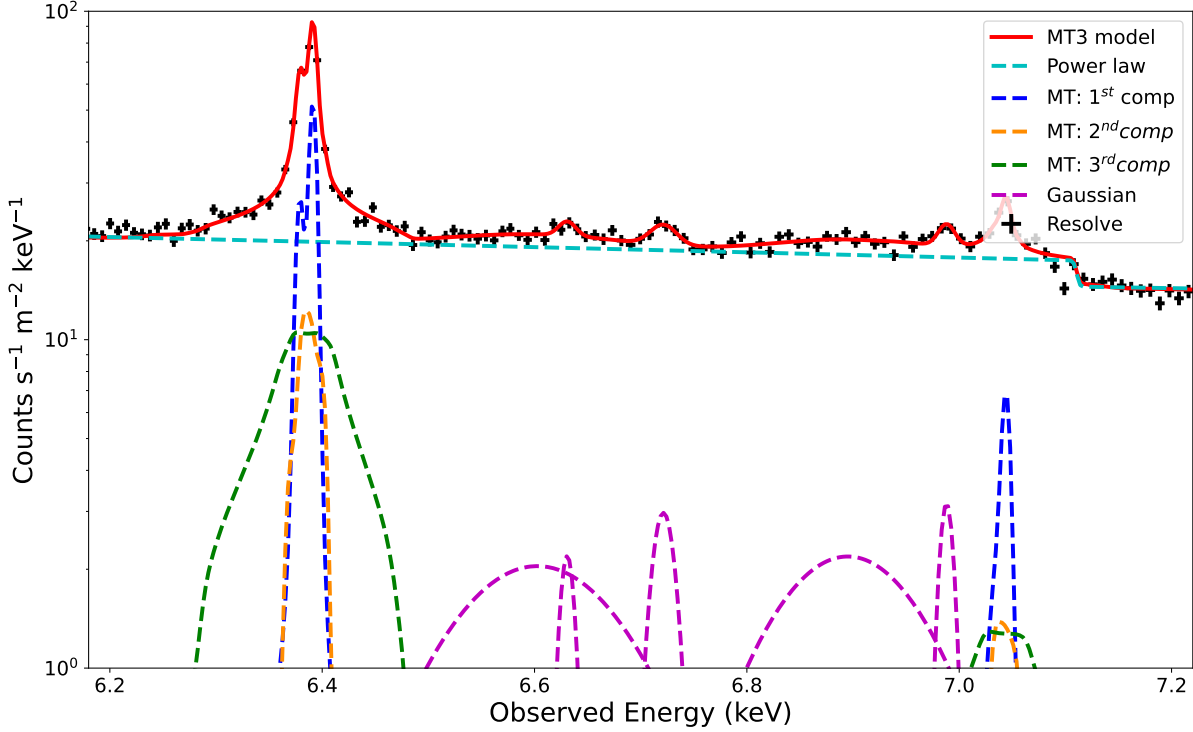


Figure 3. XRISM/Resolve (6.2 – 7.2 keV) spectra with the model curve of the MT3 plus five Gaussian model, wherein the black point, the red line, the cyan dashed-line, the blue dashed-line, the orange dashed-line, the green dashed-line, and the magenta dashed-line represent the Resolve spectra, MT3 model, power-law component, first, second, third MyTorus component, and Gaussian component, respectively. The Resolve spectrum is binned by a factor of 3 after the optimal binning for visual clarity.

factor of the absorber was fixed to $f_{\text{cov}} = 0$ for emission modeling. The covering factor of emission ($\Omega/4\pi$) was initially left free, but only a lower limit was obtained as $\Omega/4\pi > 0.17$ for all pion emission components. This is because the covering factor and column density are degenerate (L. Di Gesu et al. 2017). Therefore, we fixed the covering factor for emission to $\Omega/4\pi = 0.2$ for all the pion components.

For Doppler broadening, we adopted the `vgau` model to the pion emission component. The turbulence velocity (v_{turb}) of the pion emission component and the broadening velocity (v_{broad}) cannot be distinguished because these parameters are degenerate (J. Mao et al. 2018). Therefore, v_{turb} was fixed to be 100 km s⁻¹ (default SPEX value) and v_{broad} of the `vgau` model was left free. In summary, the free parameters for this fitting were column density (N_{H}), ionization parameter ($\log \xi$), Doppler shift velocity (v_{shift}), and broadening velocity (v_{broad}).

Although three ionized emission components were suggested, we first applied two pion models to represent the Fe-K band excess. As a result, the Doppler shift velocity were 3400 km s⁻¹ and -1500 km s⁻¹ with the broadening velocity of 3000 km s⁻¹ and 600 km s⁻¹, respectively.

The C -statistics and AICs of this model were 3643.6 and 3683.9 for the degree of freedom of 3350. Although the fit improved by adding two pion models compared to the MT3 model ($\Delta\text{AIC} = -374.1$), this model cannot explain the narrow redshifted component. Therefore, we added one more pion model component to explain the narrow/redshifted component. As a result, the statistics improved significantly ($\Delta\text{AIC} = -8.2$, Table 4). The final model is

$$\begin{aligned} & \text{hot} \times \text{reds} \times \left\{ \text{hot} \times \text{pow} + \sum_{i=1}^2 \text{gaus}_i \right. \\ & \left. + \sum_{i=1}^3 (\text{MyTorus}_i \times \text{pow} \times \text{spe}_i) \right. \\ & \left. + \sum_{i=1}^3 (\text{pion}_i \times \text{pow} \times \text{vgau}_i) \right\} \quad (4) \end{aligned}$$

We refer to this as the Narrow PION + Broad PION model (Table 4). The results of the Narrow PION + Broad PION model fitting are shown in Fig. 4, and the best-fit parameters are summarized in Table 4.

The Doppler shift velocity of the three pion emission components are 2600 ± 100 km s⁻¹ (Em1), -1400 ± 100 km s⁻¹ (Em2) and 4600^{+700}_{-800} km s⁻¹ (Em3), and the

broadening velocity of three **pion** emission components become 400_{-100}^{+200} km s⁻¹, 600_{-100}^{+200} km s⁻¹ and 3300_{-500}^{+700} km s⁻¹ for Em1, Em2 and Em3, respectively. Interestingly, the broad component (Em3) is redshifted with 4600_{-800}^{+700} km s⁻¹, indicating the ionized material is flowing. This is the first time that the ionized emission line in Cen A has been detected significantly, and the large broadening velocity indicates that Em3 is located in the inner region rather than the torus. We will discuss these features in Section 4.

Table 4. Best-fit parameters of the Narrow PION + Broad PION model.

Parameter	Unit	Narrow PION + Broad PION model
Component Em1		
pion N_{H} ⁽¹⁾	10^{22} cm ⁻²	$2.8_{-0.9}^{+1.0}$
pion $\log \xi$ ⁽²⁾	erg cm s ⁻¹	$3.10_{-0.08}^{+0.07}$
pion v_{shift} ⁽³⁾	km s ⁻¹	2600 ± 100
vgau v_{broad} ⁽⁴⁾	km s ⁻¹	400_{-100}^{+200}
Component Em2		
pion N_{H} ⁽¹⁾	10^{22} cm ⁻²	6 ± 1
pion $\log \xi$ ⁽²⁾	erg cm s ⁻¹	3.14 ± 0.04
pion v_{shift} ⁽³⁾	km s ⁻¹	-1400 ± 100
vgau v_{broad} ⁽⁴⁾	km s ⁻¹	600_{-100}^{+200}
Component Em3		
pion N_{H} ⁽¹⁾	10^{23} cm ⁻²	$1.7_{-0.4}^{+0.6}$
pion $\log \xi$ ⁽²⁾	erg cm s ⁻¹	$3.20_{-0.04}^{+0.05}$
pion v_{shift} ⁽³⁾	km s ⁻¹	4600_{-800}^{+700}
vgau v_{broad} ⁽⁴⁾	km s ⁻¹	3300_{-500}^{+700}
C -stat / d.o.f.		3627.3 / 3346
AICs		3675.7

- (1) Column density of the **pion** component. (2) Logarithm of the ionization parameter of the **pion** component. (3) Flowing velocity of the **pion** component, a positive value means the inflow and a negative value means the outflow. (4) Broadening velocity of the **vgau** component. The turbulence velocity of the **pion** component was fixed to 100 km s⁻¹, and the covering factor for emission was fixed to 0.2.

3.5.2. Collisional ionized emission modeling

Next, we replaced the **pion** model with the **cie** model (J. S. Kaastra et al. 1996). The **cie** model describes a thermal emission from a hot gas in collisional ionization equilibrium without a thermal Doppler broadening. For

the **cie** modeling, the free parameters were normalization (Y) and the electron temperature. The normalization measures $Y \equiv n_{\text{H}}n_{\text{e}}V$, where n_{H} and n_{e} are the electron and hydrogen densities and V is the volume of the source. In addition, we adopted the **vgau** model to account for thermal and other broadening effects and the **reds** model for the bulk Doppler velocity shift of the **cie** model. In summary, the model for fitting the ionized Fe-K emission lines is

$$\text{hot} \times \text{reds} \times \left\{ \text{hot} \times \text{pow} + \sum_{i=1}^2 \text{gaus}_i + \sum_{i=1}^3 (\text{MyTorus}_i \times \text{pow} \times \text{spei}_i) + \sum_{i=1}^3 (\text{cie}_i \times \text{reds}_i \times \text{vgau}_i) \right\} \quad (5)$$

We refer to this as the Narrow CIE + Broad CIE model.

The fitting result of the Narrow CIE + Broad CIE model is shown in Fig. 4, and the best-fit parameters are summarized in Table 5. The broadening velocity and the Doppler shift velocity are consistent with those of the Narrow PION + Broad PION model. Compared with the Narrow PION + Broad PION model, the Narrow CIE + Broad CIE model could not adequately explain the Fe XXVI lines (especially for the broader component, Fig. 4). The observed Fe XXVI line is stronger than the Fe XXV line for the broad component, which requires a temperature above 15 keV. On the other hand, the Fe-K emission becomes too weak to reproduce the observed line intensity for such a high temperature. Consequently, the C-statistics and AIC favor the Narrow PION + Broad PION model ($\Delta\text{AIC} = +25.8$). Thus, we considered the Narrow PION + Broad PION model to be more suitable for the 6.5–7.0 keV excess than the Narrow CIE + Broad CIE model. The broadening velocity of 550 km s⁻¹ for the narrow component is larger than the thermal broadening of Fe ions ($\sigma \sim 50$ km s⁻¹) for the best-fit temperature of 7.5 keV, indicating the presence of other broadening effects of 500 km s⁻¹.

3.5.3. Combination of the photo-ionized emission and collisional ionized emission

Finally, we tried a combination of the **pion** and **cie** models. There are two possible combinations. First, we tried the broad **cie** + narrow **pion** $\times 2$ model. However, the **cie** component could not explain the broad component for the same reason described in the Sect. 3.5.2. The narrow **pion** model components attempted to fit the residuals of the broad component instead of the narrow features. Therefore, the broad **cie** + narrow **pion** $\times 2$ model was deemed unsuitable. Next, we tried the broad

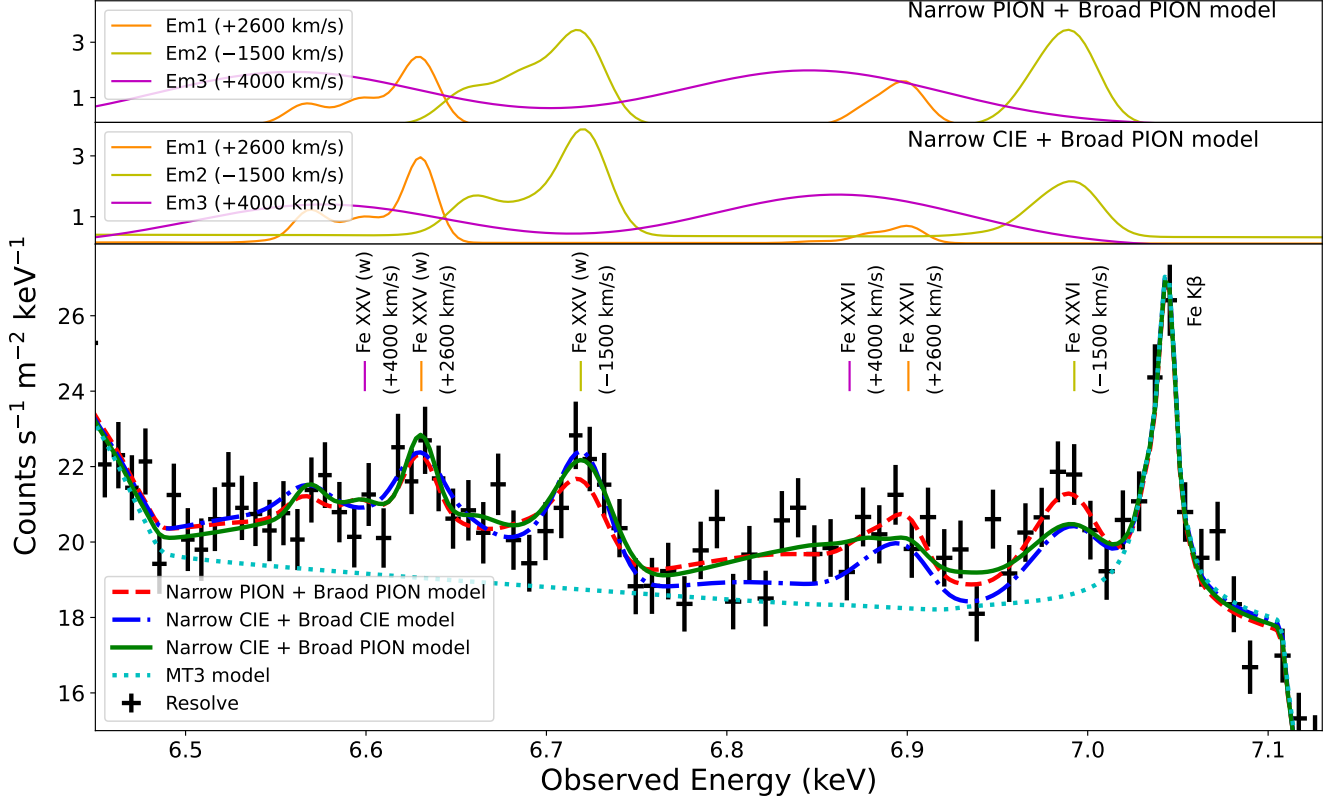


Figure 4. XRISM/Resolve (6.5 – 7.1 keV) spectra with the ionized emission model curve. The vertical and horizontal axes are the same in the top, middle, and bottom figures. Top figure: the model component curves of the Narrow PION + Broad PION model, wherein the orange line, the yellow line, and the magenta line represent the Em1 component (PIE), the Em2 component (PIE), and the Em3 component (PIE), respectively. Middle figure: the model component curves of the Narrow CIE + Broad PION model, wherein the orange line, the yellow line, and the magenta line represent the Em1 component (CIE), the Em2 component (CIE), and the Em3 component (PIE), respectively. Bottom figure: XRISM/Resolve spectra with the model curve of the Narrow PION + Broad PION model, Narrow CIE + Broad CIE model, Narrow CIE + Broad PION model, and MT3 model, wherein the black point, the red dashed line, the blue dot-dashed line, the green line, and the cyan dot line represent the Resolve spectra, Narrow PION + Broad PION model, Narrow CIE + Broad CIE model, Narrow CIE + Broad PION model, and MT3 model, respectively. The Resolve spectrum is binned by a factor of 3 after the optimal binning for visual clarity.

$\text{pion} + \text{narrow cie} \times 2$ model. This model successfully explained the 6.5–7.0 keV excess. The model for fitting the ionized Fe-K emission lines is

$$\begin{aligned}
 & \text{hot} \times \text{reds} \times \{ \text{hot} \times \text{pion}_{\text{abs}} \times \text{pow} \\
 & + \sum_{i=1}^2 \text{gaus}_i + \sum_{i=1}^3 (\text{MyTorus}_i \times \text{pow} \times \text{spe}_i) \\
 & + \sum_{i=1}^2 (\text{cie}_i \times \text{reds}_i \times \text{vgau}_i) \} \\
 & + \text{pion} \times \text{pow} \times \text{vgau} \quad (6)
 \end{aligned}$$

We refer to this as the Narrow CIE + Broad PION model.

The fitting results of the Narrow CIE + Broad PION model are shown in Fig. 4, and the best-fit parameters are summarized in Table 6. The C-statistics and AICs prefer the Narrow CIE + Broad PION model, yielding

lower values than those of the Narrow PION + Broad PION model. For the broad component, the parameters are consistent between the Narrow CIE + Broad PION model and the Narrow PION + Broad PION model. The redshift and broadening velocity of the narrow two cie components are also consistent with those of the Narrow PION + Broad PION model. Both the pion and cie models could explain the narrow ionized component (especially for Em2); however, they produce different model curves. From Fig. 4, the differences for the Em2 component are that the cie model predicts a stronger Fe xxv w line (which fits the data well), while the pion model predicts a stronger Fe xxvi line. In a photo-ionization scenario, the Fe xxv w line is typically expected to be weaker than in collisional ionization. However, assuming the different line-of-sight for the direct power-law emission and ionized component,

Table 5. Best-fit parameters of the Narrow CIE + Broad CIE model.

Parameter	Unit	Narrow CIE + Broad CIE model
Component Em1		
cie kT ⁽¹⁾	keV	8 ± 1
cie $n_{\text{H}}n_{\text{e}}V$ ⁽²⁾	10^{63} cm^{-3}	$1.7^{+1.0}_{-0.5}$
reds v_{shift} ⁽³⁾	km s^{-1}	2600 ± 100
vgau v_{broad} ⁽⁴⁾	km s^{-1}	400^{+200}_{-100}
Component Em2		
cie kT ⁽¹⁾	keV	$7.5^{+0.7}_{-0.6}$
cie $n_{\text{H}}n_{\text{e}}V$ ⁽²⁾	10^{63} cm^{-3}	$3.0^{+0.4}_{-0.5}$
reds v_{shift} ⁽³⁾	km s^{-1}	-1500 ± 100
vgau v_{broad} ⁽⁴⁾	km s^{-1}	590^{+110}_{-90}
Component Em3		
cie kT ⁽¹⁾	keV	$7.3^{+0.8}_{-0.9}$
cie $n_{\text{H}}n_{\text{e}}V$ ⁽²⁾	10^{63} cm^{-3}	$3.3^{+0.9}_{-1.3}$
reds v_{shift} ⁽³⁾	km s^{-1}	4800^{+1400}_{-800}
vgau v_{broad} ⁽⁴⁾	km s^{-1}	2500^{+800}_{-900}
C -stat / d.o.f.		3653.1 / 3346
AICs		3701.5

(1) The electron and ion temperatures. (2) Normalization of the **cie** model. (3) Doppler shift velocity of the **cie** model. Positive values represent inflow, and negative values represent outflow. (4) Broadening velocity included the effect of the thermal broadening.

the Fe XXVI w line produced by the photo-ionization can be as strong as that from collisional ionization (e.g. P. S. Woźdowski et al. 2003; S. Bianchi et al. 2005; D. Porquet et al. 2010). This is because with the different line-of-sight, the ionized component does not absorb the power-law emission, and we would instead observe scattered continuum and recombination emission. In addition, in photo-ionization, the w line intensity decreases with increasing column density (S. Bianchi et al. 2005; P. Chakraborty et al. 2021). As a result, we cannot statistically distinguish between the pure PION model and the Narrow CIE + Broad PION model; thus, we will discuss both cases below.

3.6. Modeling of the absorption line features

3.6.1. PION modeling

Table 2 shows two absorption lines above 7 keV (at 7.1 keV and 10.6 keV). In this subsection, we modeled

Table 6. Best-fit parameters of the Narrow CIE + Broad PION model.

Parameter	Unit	Narrow CIE + Broad PION model
Component Em1		
cie kT ⁽¹⁾	keV	5^{+1}_{-2}
cie $n_{\text{H}}n_{\text{e}}V$ ⁽²⁾	10^{63} cm^{-3}	$1.3^{+0.4}_{-0.3}$
reds v_{shift} ⁽³⁾	km s^{-1}	2600 ± 100
vgau v_{broad} ⁽⁴⁾	km s^{-1}	400 ± 100
Component Em2		
cie kT ⁽¹⁾	keV	$7.5^{+0.8}_{-0.7}$
cie $n_{\text{H}}n_{\text{e}}V$ ⁽²⁾	10^{63} cm^{-3}	$2.8^{+0.5}_{-0.4}$
reds v_{shift} ⁽³⁾	km s^{-1}	-1500 ± 100
vgau v_{broad} ⁽⁴⁾	km s^{-1}	550^{+110}_{-80}
Component Em3		
pion N_{H} ⁽⁵⁾	10^{23} cm^{-2}	$1.8^{+0.5}_{-0.4}$
pion $\log \xi$ ⁽⁶⁾	erg cm s^{-1}	$3.23^{+0.05}_{-0.04}$
pion v_{shift} ⁽⁷⁾	km s^{-1}	4000 ± 500
vgau v_{broad} ⁽⁸⁾	km s^{-1}	3100 ± 500
C -stat / d.o.f.		3617.6 / 3346
AICs		3666.0

(1) The electron and ion temperatures. (2) Normalization of the **cie** model. (3) Doppler shift velocity of the **cie** model. Positive values represent inflow, and negative values represent outflow. (4) Broadening velocity. (5) Column density of the **pion** component. (6) Logarithm of the ionization parameter of the **pion** component. (7) Flowing velocity of the **pion** component, a positive value means the inflow and a negative value means the outflow. (8) Broadening velocity of the **vgau** component which included the thermal broadening. The turbulence velocity of the **pion** component was fixed to 100 km s^{-1} , and the covering factor for emission was fixed to 0.2.

them with the **pion** absorption model (J. M. Miller et al. 2015; M. Mehdipour et al. 2016). Spectral fitting was performed by adding a **pion** absorption model to the Narrow CIE + Broad PION model described above to save computing time. For the **pion** absorption modeling, the free parameters were the hydrogen column density N_{H} (cm^{-2}), ionization parameter $\log \xi$ (erg cm s^{-1}), outflow velocity v_{out} (km s^{-1}) and turbulence velocity v_{turb} (km s^{-1}). We started with a single-zone photoionized absorber to express these absorption lines

individually (Table 7). The model is

$$\begin{aligned} & \text{hot} \times \text{reds} \times \{\text{hot} \times \text{pion}_{\text{abs}} \times \text{pow} \\ & + \sum_{i=1}^2 \text{gaus}_i + \sum_{i=1}^3 (\text{MyTorus}_i \times \text{pow} \times \text{spei}_i) \\ & + \sum_{i=1}^2 (\text{cie}_i \times \text{reds}_i \times \text{vgau}_i) \\ & \quad + \text{pion} \times \text{pow} \times \text{vgau} \} \quad (7) \end{aligned}$$

When leaving the covering factor C_f of the absorber free, the C -stat did not improve. Therefore, C_f of all absorption **pion** was fixed to 1. Table 7 summarizes the result of fitting only the 7.1 keV line (A1a model, Fig. 5) and only the 10.6 keV line (Fig. 6). There are two fitting results for each 7.1 keV and 10.6 keV absorption line. One is the H-like Fe (Fe XXVI) case (A1b model and A1d model), and another is the He-like Fe (Fe XXV) case (A1a model and A1c model). The above four models improved the C -statistics and the AIC significantly over the Narrow CIE + Broad PION model, and thus it can be considered that these **pion** components are significant. We found the wind outflows in a jet-dominated object. In the A1b and A1d models (H-like Fe case), the column density of the second **MyTorus** moved to the lower limit ($1.1 \times 10^{22} \text{ cm}^{-2}$). This is because the column density of **pion** is as large as $2 \times 10^{24} \text{ cm}^{-2}$ and thus the incident power-law component should be heavily absorbed. Then, the best-fit power-law normalization became large by a factor of ~ 10 . On the other hand, the line flux of the **MyTorus** is not affected by the **pion** absorber. Consequently, the relative line flux ratio to the incident power-law becomes smaller. This normalization is also tied to that of **MyTorus**, and thus the column density is forced to become smaller to reproduce the small line flux ratio.

When compared statistics, the A1b model was better than the A1a model ($\Delta C = -72.5$ and $\Delta \text{AIC} = -72.5$), and the A1d model was better than the A1c model ($\Delta C = -51.4$ and $\Delta \text{AIC} = -51.4$). When we compared with the C -stat of the Resolve, the A1b model was better than the A1a model ($\Delta C = -9.6$), and the A1d model was better than the A1c model ($\Delta C = -1.2$). Then, we compared the C -stat of the limited band for Resolve. For the A1a and A1b model, the C -stat of the 6.5 – 7.6 band keV was 436.7 and 441.6. When we focused on the 7.1 keV absorption line, the A1a (He-like) model was preferred; however, the C -stat of the total Resolve band preferred the A1b (H-like) model. This is because the C -stat of the 5 – 6.2 keV band was 518.5 (A1a model) and 487.1 (A1b model), and the A1b model is significantly preferred ($\Delta C = -31.3$). A similar trend is present even for the 10.6 keV absorption line. The C -stat of the

9.5 – 12 keV band for the A1c and A1d model was 632.8 and 635.0. However, for the A1c and A1d model, the C -stat of the 5 – 6.2 band keV was 520.3 and 494.6. As a result, when we focused on the absorption lines, the He-like case (A1a and A1c model) is preferred, but the 5 – 6.2 keV band preferred the H-like case (A1b and A1d model).

C -stat of the Resolve for each model is 3179.4 (A1a), 3169.8 (A1b), 3181.4 (A1c), and 3180.1 (A1d). The total C -stat of the H-like case significantly improved than the He-like case (for both 7.1 keV and 10.6 keV absorption lines); however, the C -stat of the Resolve is less different. This suggests there are significant differences in the NuSTAR spectra. There is no significant difference in the model curve within the Resolve band (Fig. 14). The slight differences lie in the presence of weaker absorption lines in the Resolve band and above the 40 keV band. This is because the A1d model has a very large column density, so even at high ionization, the continuum is reduced by scattering. However, increasing the power-law normalization by a factor of 10 to counteract the scattering effect renders the two model curves visually indistinguishable. However, as we discuss in subsection 4.2, the upper limit of position for the A1b model and A1d models (Fe XXVI case) is inside the ISCO.

As a result, we could not simply determine whether Fe XXV and Fe XXVI for these absorption lines. The total C -stat preferred Fe XXVI; however, the C -stat of the limited band for Resolve, which is focused on the absorption line, and their radius preferred Fe XXV.

Next, we tried the combination of two components. When the multiple components of the **pion** model are considered, the first component sees the non-absorbed SED, and the second component sees the absorbed SED (absorbed by the first component). The position setting for the multiple components of the **pion** model component was determined with the faster 10.6 keV component positioned inside. We tested four cases, Fe XXV and Fe XXVI, for each of the two absorption lines. The model for the combination of two **pion** absorption components is expressed as

$$\begin{aligned} & \text{hot} \times \text{reds} \times \{\text{hot} \times \text{pion}_{\text{abs}} \times \text{pion}_{\text{abs}} \times \text{pow} \\ & + \sum_{i=1}^2 \text{gaus}_i + \sum_{i=1}^3 (\text{MyTorus}_i \times \text{pow} \times \text{spei}_i) \\ & + \sum_{i=1}^2 (\text{cie}_i \times \text{reds}_i \times \text{vgau}_i) \\ & \quad + \text{pion} \times \text{pow} \times \text{vgau} \} \quad (8) \end{aligned}$$

This model is simply the combination of the two absorbers. The fitting results about the combination of two **pion** absorption components are shown in Table 7. The

A2a model means the combination of the A1a and A1c model, the A2b model means the combination of the A1a and A1d model, the A2c model means the combination of the A1c and A1c model, and the A2d model means the combination of the A1b and A1d model. From the C -stat and AICs, the combination of the two pion absorption components gave a significantly better fit than the one pion absorption component.

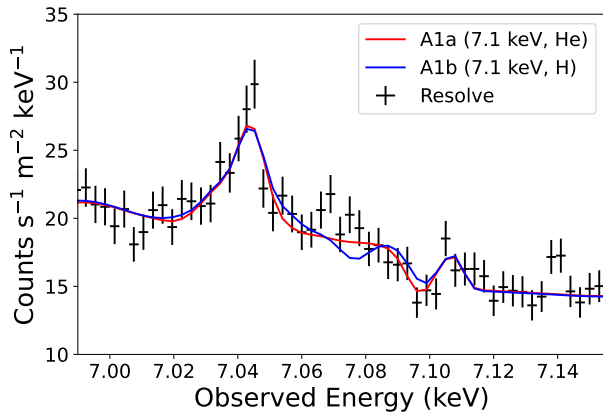


Figure 5. Resolve spectra (6.9 – 7.1 keV) and model curve of the A1a model and A1b model, wherein the black point, the red line, and the blue line represent the Resolve spectra, A1a model, and A1b model, respectively.

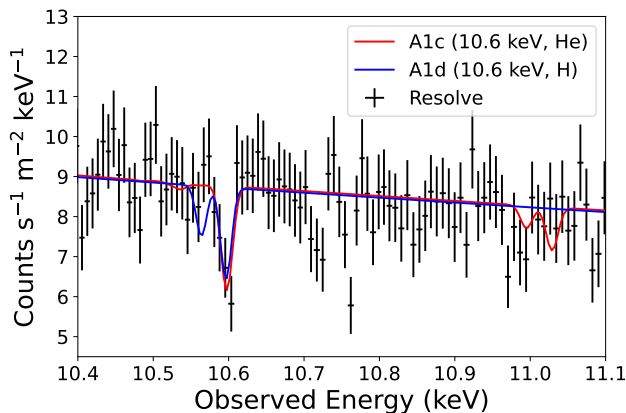


Figure 6. Resolve spectra (10.4 – 11.1 keV), model curve of the A1d model and A1c model, wherein the black point, the red line, and the blue line represent the Resolve spectra and A1d model and A1c, respectively. The Resolve spectrum is binned by a factor of 2 after the optimal binning for visual clarity.

To evaluate whether NuSTAR data drives the preference for certain models. We removed the NuSTAR spectrum from the analysis and fitted the spectrum with

Resolve only (3 – 15 keV). Then, the parameters of the ionized emission changed (specifically, the broadening velocity of the narrow (redshift) component increased from 400 km s^{-1} to 2000 km s^{-1}). This is because, when using only the Resolve data (3 – 15 keV), since hard X-rays are excluded, the continuum shape is altered to account for the excess in the Fe-K band. Then, we fixed the broadening velocities of the ionized emission components and fit the Resolve spectrum using the A1a and A1c models. When the A1a model is applied, the photon index $\Gamma = 1.858$ changes to $\Gamma = 1.915$, and when the A1c model is applied, the photon index $\Gamma = 1.857$ changes to $\Gamma = 1.909$. However, the parameters of the absorption components are not changed significantly. As a result, the broadening velocity of the narrow component is sensitive to the continuum shape. Thus, some uncertainties in the distance estimation of the narrow ionized emission component.

3.6.2. Fe-K absorption edge modeling for 7.1 keV absorption line feature

The 7.1 keV absorption line can be superimposed on the Fe-K edge structure. Therefore, it could appear as an artifact if the Fe-K edge is not well modeled; that is, if the model shape does not accurately reproduce the edge energy and shape. Here, we investigated two alternative cases for Fe-K edge modeling: the `am01` model for the dust (molecular) absorption and a Doppler-shifted `hot` model. The `am01` model calculates transmission through molecular absorbers (C. Pinto et al. 2010; D. Rogantini et al. 2018). We applied the `am01` model to the power-law component. For the `am01` fitting, the range of Fe abundance in the `hot` model was set to 0 – 0.2, the assumption that up to 20% of Fe is not contained in the dust. This is a typical value for the Milky Way (e.g. I. Psaradaki et al. 2023). We can choose molecules in the `am01` model that could produce a Fe-K edge, and we tried all of them. As a result, the choice of Troilite (FeS) molecule gave the best C -stat and AICs (C -stat is 3601.0 and AICs is 3653.4). The best-fit parameters are summarized in Table 8. However, compared to the A1a model, the statistics were not favorable, and thus the `am01` modeling could not account for the 7.1 keV absorption line (-like) structure (Fig. 7). As seen in the figure, the `am01` model gives a lower edge energy than `hot` and a slightly different edge shape, but cannot explain the 7.1 keV absorption line feature. There are various dust models (e.g., C. Ricci & S. Paltani 2023), but the trend is almost similar; the edge energy decreases with a slight change in edge shape. Therefore, we consider that these models do not explain the 7.1 keV absorption line feature.

Table 7. Best-fit of pion absorption models.

Model	Comp.	N_{H} (10^{21} cm^{-2})	$\log \xi$ (erg cm s^{-1})	v_{out} (km s^{-1})	v_{turb} (km s^{-1})	C-stat	d.o.f.	AIC
A1a	7.1 keV (He)	1.5 ± 0.4	$2.91^{+0.09}_{-0.07}$	-17790^{+80}_{-60}	160^{+90}_{-70}	3596.0	3342	3652.5
A1b	7.1 keV (H)	$(2.1 \pm 0.1) \times 10^3$	5.9 ± 0.1	-5890 ± 70	< 230	3523.5	3342	3580.0
A1c	10.6 keV (He)	5 ± 2	3.3 ± 0.1	-129010^{+50}_{-60}	200^{+70}_{-50}	3591.2	3342	3647.7
A1d	10.6 keV (H)	$(2.0 \pm 0.1) \times 10^3$	5.8 ± 0.1	-119080^{+60}_{-70}	160 ± 70	3539.8	3342	3596.3
A2a	7.1 keV (He)	1.5 ± 0.4	$2.91^{+0.09}_{-0.07}$	-17780^{+80}_{-60}	160^{+90}_{-70}	3569.3	3338	3633.3
	10.6 keV (He)	5 ± 2	3.3 ± 0.1	-129010^{+50}_{-60}	200^{+70}_{-50}			
A2b	7.1 keV (He)	$1.6^{+0.5}_{-0.4}$	2.89 ± 0.08	-17790^{+70}_{-60}	160^{+80}_{-70}	3516.9	3338	3581.5
	10.6 keV (H)	$(2.1 \pm 0.1) \times 10^3$	5.8 ± 0.1	-119010^{+60}_{-70}	160 ± 70			
A2c	7.1 keV (H)	5^{+4}_{-2}	$3.4^{+0.2}_{-0.1}$	-5860 ± 50	< 190	3604.8	3338	3669.4
	10.6 keV (He)	$(2.0^{+0.1}_{-0.2}) \times 10^3$	5.8 ± 0.1	-119080^{+60}_{-70}	160 ± 70			
A2d	7.1 keV (H)	$(2.1 \pm 0.1) \times 10^3$	5.9 ± 0.1	-5890 ± 70	< 230	3505.5	3338	3561.9
	10.6 keV (H)	$(0.2^{+1.1}_{-0.1}) \times 10^2$	$4.1^{+0.4}_{-0.2}$	-119060 ± 70	190^{+70}_{-60}			

N_{H} : Column density. $\log \xi$: Logarithm of the ionization parameter. v_{out} : Outflow velocity. v_{turb} : Turbulence velocity.

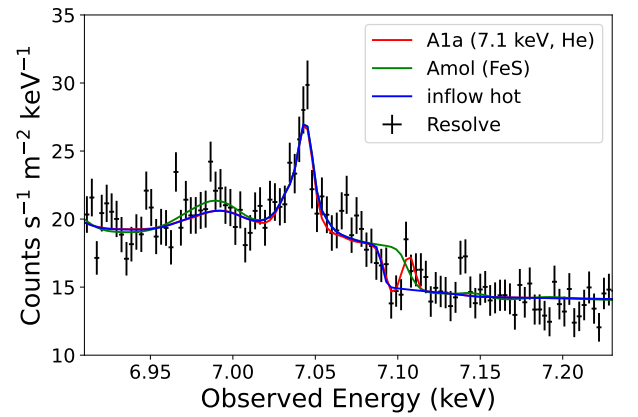
Next, we tried the Doppler-shifted **hot** model to change the edge energy by allowing the shift velocity of **hot** in the Narrow CIE + Broad PION model to vary. As summarized in Table 8, the redshift velocity becomes $v_{\text{flow}} = +810^{+170}_{-90} \text{ km s}^{-1}$. The C -stat was 3603.2, and the AIC was 3635.6. When we compared this model with the A1a pion model, the ΔAIC was 1.1 (slightly favoring the A1a model). The column density of this model was $(1.655^{+0.008}_{-0.007}) \times 10^{23} \text{ cm}^{-2}$; therefore, we considered that this absorption originates from the torus (e.g., Y. Fukazawa et al. 2011). This indicates a fast inflow of torus material. On the other hand, there is no evidence of such inflow at other wavelengths for Cen A. H. Zhou et al. (2019) reported the detection of inflowing gas with $5,000 \text{ km s}^{-1}$ for quasars, suggesting that it is flowing at ~ 1000 gravitational radius. The Eddington ratio of Cen A is as small as $\sim 10^{-3}$, and such a massive inflow with a column density of $\sim 10^{23} \text{ cm}^{-2}$ at a small radius is unlikely. Fig. 7 shows that the inflowing **hot** model cannot explain the excess count around 7.11 keV, and thus the **pion** A1a model gives better statistics as seen in Table 8. Therefore, we considered the **pion** model to be more suitable for the 7.1 keV structure.

4. DISCUSSION

XRISM/Resolve observations revealed that several ionized Fe-K emission or absorption lines with a shift velocity and a width in the range of $10^{2-5} \text{ km s}^{-1}$ are present in the X-ray spectrum of Cen A. Some of the ionized Fe-K emission lines are redshifted. To discuss their

Table 8. Best-fit parameters of modeling the 7.1 keV structure.

	pion (A1a)	amol (FeS)	Inflow hot
$N_{\text{H}} (\times 10^{22} \text{ cm}^{-2})$	0.15 ± 0.04	$(4.62 \pm 0.02) \times 10^{-4}$	$16.55^{+0.08}_{-0.07}$
$v_{\text{flow}} (\text{km s}^{-1})$	-17790^{+80}_{-60}	0	$+810^{+170}_{-90}$
C -stat	3596.0	3601.0	3603.2
AICs	3652.5	3653.4	3653.6

**Figure 7.** XRISM/Resolve (6.95 – 7.25 keV) spectra with the model curve of the A1a model, **amol** model, and inflowing **hot** model, wherein the black point, the red line, the green line, and the blue line represent the Resolve spectra, the model curve of the A1a model, **amol** model, and inflowing **hot** model, respectively.

origins, we estimate physical quantities calculated from the obtained ionization parameter and column density for the `pion` model or the emission measure for the `cie` model.

The ionization parameter is defined as in Eq. (1). The ionization luminosity (L_{ion}) is calculated from the best-fit power-law model to be 5×10^{42} erg s $^{-1}$. Since the distance of the gas from the ionizing source (r) is larger than the depth d of the gas along the line of sight ($r > d$) and the column density is $N_{\text{H}} = nd$, we can obtain an upper limit on the distance as $r < \frac{L}{\xi N_{\text{H}}}$. The mass flow rate is calculated as $\dot{M}_{\text{flow}} = 4\pi\mu m_p r N_{\text{H}} C_v v$ (D. M. Crenshaw et al. 2003; D. M. Crenshaw & S. B. Kraemer 2012; F. Tombesi et al. 2017; L. C. Gallo et al. 2023), where $\mu = 1.23$ is the mean atomic mass per proton, m_p is the proton mass, and v is the flow (redshift or blueshift) velocity. The covering factor $\Omega/4\pi$ is assumed to be 0.2 for the emission line. The kinetic power is $\dot{E}_{\text{kinetic}} = \frac{1}{2}\dot{M}v^2$ (F. Tombesi et al. 2013).

In the case of the `cie` model, assuming a typical size of the plasma as R , the number density of the gas is calculated as $n = \sqrt{\frac{EM}{qR^3}}$, where EM is the emission measure and q is a geometrical factor. Then, the total mass of the gas is $M_{\text{gas}} = \mu m_p n q R^3$, the mass flow rate is $\dot{M}_{\text{flow}} = \mu m_p n q R^3 v$, the kinetic power is $\dot{E}_{\text{kinetic}} = \frac{1}{2}\dot{M}_{\text{flow}}v^2$, and the thermal energy is $E_{\text{thermal}} = nkTqR^3$.

Table 9 summarizes the obtained parameters and the calculated plasma quantities, where we show the dependence on r , C_v , or q , R . For the narrow emission lines, there are two components, but here we treat them in the same manner by using the parameters as shown in the table. Note that the black hole mass of Cen A is $(5.5 \pm 3.0) \times 10^7 M_{\odot}$, and thus the Eddington luminosity is 6.9×10^{45} erg s $^{-1}$. The 2 – 10 keV luminosity of the power-law component is 2.07×10^{42} erg s $^{-1}$ (derived from the A1a model after correcting for absorption). To estimate the bolometric luminosity, we use the 1 – 1000 Ryd luminosity (L_{ion}) of the power-law component as the lower limit and the bolometric correction factor $\kappa_{2-10} = 20$ (R. V. Vasudevan & A. C. Fabian 2007) relative to the 2 – 10 keV power-law luminosity as the upper limit, because Cen A is a low Eddington ratio AGN. The 1 – 1000 Ryd (13.6 eV – 13.6 keV) luminosity (L_{ion}) of the power-law component from the A1a model is $L_{\text{ion}} = 6.65 \times 10^{42}$ erg s $^{-1}$ (we could obtain the same luminosity using the A1c model). Thus, the upper limit of the bolometric luminosity is $L_{\text{bol}} = 4.1 \times 10^{43}$ erg s $^{-1}$, and the lower limit is $L_{\text{bol}} = 6.7 \times 10^{42}$ erg s $^{-1}$. The Eddington ratio is estimated to be $\lambda = 0.001 - 0.006$. The Eddington mass flow rate is $\dot{M}_{\text{Edd}} = 1.22 M_{\odot} \text{ yr}^{-1}$.

4.1. Ionized emission lines

We detected three ionized emission components in Cen A. XRISM has observed some AGNs in the PV phase, including two low-luminosity AGNs: M81* and Cen A. The M81* XRISM observation detected two ionized Fe-K emission components with widths of 800 km s $^{-1}$ and 200 km s $^{-1}$, and redshifted velocities of 170 km s $^{-1}$ and 1500 km s $^{-1}$, respectively (J. M. Miller et al. 2025). However, the ionization mechanism for the two components in M81* was not determined (photo-ionization or collisional ionization). In Cen A, both photo-ionized and collisionally ionized plasma models can represent the two narrow ionized components, while the origin of the broad ionized component is likely photo-ionization (as described by the `pion` model). Such ionized emission line components might be a common feature of low-luminosity AGNs, but their physical properties differ between Cen A and M81*.

4.1.1. Broad redshifted ionized emission

From the Table 9, the upper limit on the distance from the ionizing source is as small as $1300 R_{\text{S}}$. This is because the ionizing luminosity (5×10^{42} erg s $^{-1}$) is relatively low compared to the other XRISM observed UFO AGNs (e.g., Xrism Collaboration et al. 2025; M. Mehdipour et al. 2025; H. Noda et al. 2025). In this case, the gravitational redshift is larger than 110 km s $^{-1}$ and thus cannot be ignored relative to the apparent redshift velocity of 4600 km s $^{-1}$ (and would be larger if the distance were smaller).

Inflow, outflow, or rotation with a disk-like or spherical shape is expected to show a double-peak emission line profile, centered on the source-rest-frame line energy. Therefore, if the flow is disk-like or spherical, an alternative interpretation is that the observed shift is purely gravitational (4600 km s $^{-1}$), which would place the emitting material at a distance from the central black hole of $r \sim 30 R_{\text{S}}$. The line width of ~ 3000 km s $^{-1}$ might represent a range of inflow or outflow velocity that blends the double-peak profile into a broad single peak. The escape velocity at this radius is 5.5×10^4 km s $^{-1}$, indicating that the flow would require supporting energy to keep the gas at this radius against the gravitational force (or if it were an outflow, it would fail to escape). A past period of high activity of the central engine might have ejected an outburst of gas, and its kinetic energy might now be supporting the gas.

One possibility of making a single line profile is that the blueshifted outflow component on the near side is obscured by the torus, leaving only the redshifted component on the far side visible. But r is so small that the emitter will be seen to be almost point-like from the

Table 9. Calculated physical quantities.

	Unit	Broad component		Narrow component		UFO _{7.1 keV}	UFO _{10.6 keV}
Shift velocity	km s ⁻¹	4600		2600, -1500		-17790	-129010
Broadening velocity	km s ⁻¹	3300		400, 600		150	190
Column density	cm ⁻²	1.7 × 10 ²³		3 × 10 ²²		1.5 × 10 ²¹	4 × 10 ²¹
Ionization parameter	erg cm s ⁻¹	3.2		3.1		2.9	3.3
Ionization mechanism		PIE		PIE			CIE
Radius ^a	R _S	-		-		500 ($\frac{n_H}{10^8 \text{cm}^{-3}}$) ^{-0.5}	330 ($\frac{n_H}{10^8 \text{cm}^{-3}}$) ^{-0.5}
Lower limit Radius ^b	R _S	-		-		2.8 × 10 ²	5.4
Upper limit Radius ^c	R _S	1300		8 × 10 ³		2.7 × 10 ⁵	3.5 × 10 ⁴
Mass-flow rate	M _⊙ yr ⁻¹	0.01 ($\frac{r}{100 R_S}$)		0.008 ($\frac{r}{10^3 R_S}$)		0.04 q ($\frac{r}{0.5 \text{pc}}$)	2 × 10 ⁻⁴ ($\frac{r}{100 R_S}$) ($\frac{C_v}{0.1}$)
Kinetic power	erg s ⁻¹	1 × 10 ⁴¹ ($\frac{r}{100 R_S}$)		1 × 10 ⁴¹ ($\frac{r}{10^3 R_S}$)		5.3 × 10 ⁴⁰ q ^{1.5} ($\frac{r}{0.5 \text{pc}}$) ^{1.5}	4 × 10 ⁴⁰ ($\frac{r}{100 R_S}$) ($\frac{C_v}{0.1}$)

a: Radius, assuming the Keplerian motion using the broadening velocity. b: Lower limit of the radius using the $r_{\min} = 2GM_{\text{BH}}/v_{\text{out}}^2$. c: Upper limit of the radius using the $r_{\max} = L_{\text{ion}}C_v/\xi N_{\text{H}}$, where $C_v = 1$ is the volume filling factor.

torus, and thus both the near and far sides would likely be either obscured or unobscured together.

Another possibility is that the flow is not disk-like or spherical, but the geometry is such that only redshifted emission is observed; for example, an inflow at a large angle relative to the disk. As discussed in [D. Bogensberger et al. \(2025\)](#), the viewing angle of Cen A is uncertain but may be around 20–70 degrees. In that case, most of the flow region would show a redshift. One scenario to explain such a flow is a failed outflow [C. Li et al. \(2025\)](#). In this case, the distance from the central black hole could be as large as 1300 R_S and the mass flow rate becomes 0.1 $M_{\odot} \text{ yr}^{-1}$. A high activity in the past could have produced such a massive outflow. In summary, the broad emission component is not straightforwardly understood.

4.1.2. Narrow ionized emission

XRISM/Resolve revealed both blueshifted and redshifted narrow ionized emission components in the Fe-K band, and their shift velocities are similar ($\sim 2000 \text{ km s}^{-1}$). We cannot rule out the possibility of two different velocity components, but here we consider them to share the same origin for simplicity, indicating that the gas geometry is disk-like or spherical.

If the gas is a photoionized plasma, the upper limit on its distance from the central ionizing source is $8 \times 10^3 R_S$. The gravitational redshift is $\sim 21 (8 \times 10^3 R_S/r) \text{ km s}^{-1}$ and the escape velocity is $\sim 3400 (8 \times 10^3 R_S/r)^{0.5} \text{ km s}^{-1}$. Thus, the gravitational redshift could explain the small difference in velocity between the redshifted and blueshifted components if the distance is as large as $r \sim 10^3 R_S$. The observed velocity is not much lower than the escape velocity, and thus, either inflow, outflow, or rotation can be considered. Then, the mass flow rate would be $0.008 M_{\odot} \text{ yr}^{-1}$ ($0.006 \dot{M}_{\text{Edd}}$), close to that estimated from the current Cen A luminosity. The kinetic

power of the flow is estimated to be $\dot{E}_{\text{kinetic}} = 1.1 \times 10^{40} \text{ erg s}^{-1}$. This could be driven by the current AGN activity.

The upper limit on the mass flow rate of these components is estimated to be $\dot{M}_{\text{blue}} = 0.006 M_{\odot} \text{ yr}^{-1}$. The upper limit on the kinetic power is estimated to be $\dot{E}_{\text{blue}} = 1 \times 10^{41} \text{ erg s}^{-1}$.

In the case of a collisional ionized plasma, we cannot constrain the distance from the center, but its emission must originate from a region obscured by the torus; otherwise, their emission should appear in the soft X-ray band without absorption. Therefore, the plasma is likely located within the torus region of $< 1 \text{ pc}$. In addition, since the thermal broadening is at most 50 km s^{-1} for the temperature of 7 keV, other broadening mechanisms, such as turbulence, must contribute with 400 km s^{-1} . Assuming a typical size of $r = 0.5 \text{ pc}$, we obtain a gas number density of $n_{\text{blue}} \sim 3.0 \times 10^3 \text{ cm}^{-3} q^{-1.5} (r/0.5 \text{ pc})^{-1.5}$, a total gas mass $M = 7.4 \times 10^{-2} q^{1.5} (r/0.5 \text{ pc})^{1.5} M_{\odot}$, and a total thermal energy $E_{\text{thermal}} = 2.9 \times 10^{52} q^{1.5} (r/0.5 \text{ pc})^{1.5} \text{ erg}$. The escape velocity is around 940 km s^{-1} , and thus outflow or rotation are also possibilities, in addition to inflow. In the outflow or rotation case, the plasma would be produced if a part of the accreting matter (BLR, torus, or others) was shock-heated by a massive AGN outflow. The total thermal energy can be supplied by the current AGN power within 10^3 yr . The total mass is smaller than that expected for the torus region, suggesting that only a part of the circumnuclear matter might be heated. The mass flow rate is $0.04 q (r/0.5 \text{ pc}) M_{\odot} \text{ yr}^{-1}$ ($0.03 \dot{M}_{\text{Edd}}$) and the kinetic power is $5.3 \times 10^{40} q^{1.5} (r/0.5 \text{ pc})^{1.5} \text{ erg s}^{-1}$. Therefore, the current AGN activity is sufficient to drive the outflow.

Another possibility is an outer region of radiatively inefficient accretion flow (RIAF; [E. Quataert & R. Narayan 1999](#)) inflow since Cen A is a low Eddington

AGN ($L/L_{\text{Edd}} \sim 10^{-3}$; Y. Fukazawa et al. 2016; Y. Nakatani et al. 2023; T. Iwata et al. 2024; D. Bogensberger et al. 2024). While the innermost regions of the RIAF are expected to be at high temperature with fully ionized gas, the outer region could remain cool enough to allow Fe XXV and Fe XXVI to exist. The two narrow components might correspond to the inflowing RIAF wind (F. Shi et al. 2021, 2025). In the case of the RIAF inflow, the mass flow rate is estimated as $\dot{M} = 0.4M_{\odot} \text{ yr}^{-1}$, which is too high for RIAF.

4.2. Ionized absorption lines

The 10.6 keV component has a significantly faster outflowing velocity than the 7.1 keV component. Therefore, the 10.6 keV component should be located within the inner of the 7.1 keV component, and we set the relation of the model components so in the fitting. Considering the inner π ion component has a higher (or the same) Hydrogen number density, the inner component should have a higher ionization degree than the outer component. However, the 10.6 keV component has a significantly lower ionization degree than the 7.1 keV component in the A2d model. Thus, the A2d model (Fe XXVI for both absorption lines) might not suit the model. Moreover, the inner component should be more highly ionized than the outer component. Therefore, the A2c model (Fe XXVI for the 7.1 keV component and Fe XXV for the 10.6 keV component) might also not suit the model.

Assuming that the wind has a faster outflow velocity v_{out} than the escape velocity, the lower limit on the position of the ionized wind was evaluated as $D_{\text{min}} = 2GM_{\text{BH}}/v_{\text{out}}^2$, using the outflow velocity v_{out} . The evaluated upper limit and lower limit distances from the SMBH for all two π ion absorption model cases are listed in Table 10. The upper limit distance in the A2b, A2c, and A2d models is the inner ISCO; therefore, it is physically unlikely for wind to flow from that radius. In addition, the upper and lower limits in the A2b, A2c, and A2d models are inconsistent, which suggests that the winds are failed winds (e.g., D. Proga & T. R. Kallman 2004) or that the A2b, A2c, and A2d models are not suitable for physical interpretation. This inconsistency (upper limit distances from the SMBH are inside the ISCO) is due to their high column density (above 10^{24} cm^{-2}). In the π ion model, the continuum component counteracts the scattering effect, increasing the power-law normalization by a factor of 10. This behavior is also seen in using the `xabs` model in SPEX code. From the past broadband Cen A observations (A. Borkar et al. 2021), the bolometric luminosity was computed to $L_{\text{bol}} = 9.45 \times 10^{42} \text{ erg s}^{-1}$. In the A1a model

(or A1c model; both cases have similar luminosity), the 2–10 keV luminosity is consistent with past CCD observations (e.g., obtained using the *Swift*/BAT). However, the power-law normalization in the models considering the H-like absorption line became larger by a factor of ~ 10 than that of the He-like absorption line case. Despite the ionization degree being very large at $\log \xi = 5.8 \text{ erg cm s}^{-1}$, a significant difference appears in the continuum flux because the Hydrogen column density is large ($N_{\text{H}} = 2 \times 10^{24} \text{ cm}^{-2}$), leading to Compton scattering. From the power-law normalization of the A1b models (or the A1d model; both cases have similar luminosity), the 2–10 keV luminosity is $1.1 \times 10^{43} \text{ erg s}^{-1}$ after correcting for absorption. This significantly high luminosity, with the models considering the H-like absorption line, might be physically unlikely. Although this might be model-dependent. While the scattering is treated as energy-independent Thomson attenuation, effectively acting as a grey absorber, without Klein-Nishina effects or Compton energy redistribution, and all scattered photons are treated as lost. Such an approximation can overestimate continuum suppression at high column densities and may artificially require a higher power-law normalization to fit the data. As a result, the inferred ~ 10 times normalization increase could reflect limitations of the radiative transfer treatment rather than a physical inconsistency of the Fe XXVI solution. As a result, we do not reject the Fe XXVI. Since the A2b, A2c, and A2d models using the π ion model might be physically unlikely. Hereafter, for the discussion, we use parameters from the model considering the He-like absorption line.

The Eddington ratio is estimated to be $\lambda = 0.001 - 0.006$ (Sect. 4). This Eddington ratio is too small for the line-force mechanism (e.g., S. A. Sim et al. 2010; M. Nomura & K. Ohsuga 2017). On the other hand, the outflow velocity is too high for a thermally driven wind (e.g., C.-A. Faucher-Giguère & E. Quataert 2012; M. Mizumoto et al. 2019a). Thus, either line-driven or thermal-driven wind launch mechanism is unlikely to be. For these reasons, the wind driving mechanism is thought to be Magneto-Hydrodynamics (MHD) driving. In this case, the shape of the absorption line is predicted to be asymmetric (P. Gandhi et al. 2022; R. Tomaru et al. 2023), but current data do not allow us to study this possibility.

From the simulations, if the ratio of wind kinetic power to their bolometric luminosity is above $\sim 5\%$ (and can be as low as $\sim 0.5\%$), the wind can contribute to host galaxy feedback (e.g. T. Di Matteo et al. 2005). In addition, quasi-analytical studies suggest that disk winds may promote the collimation of jets near SMBHs (K. Fukumura et al. 2014; N. Globus & A. Levinson 2016;

Table 10. Evaluated radius from the absorption models.

	A2a		A2b		A2c		A2d	
	7.1 keV (He)	10.6 keV (He)	7.1 keV (He)	10.6 keV (H)	7.1 keV (H)	10.6 keV (He)	7.1 keV (H)	10.6 keV (H)
L_{ion}/ξ ⁽¹⁾	642	278	162	5.25	225	5.21	4.37	265
N_{H} ⁽²⁾	1.5 ± 0.4	5 ± 2	$1.6_{-0.4}^{+0.5}$	$(2.1 \pm 0.1) \times 10^3$	5_{-2}^{+4}	$(2.1 \pm 0.1) \times 10^3$	$(2.1 \pm 0.1) \times 10^3$	$(0.2_{-0.1}^{+1.1}) \times 10^2$
v_{out} ⁽³⁾	-17780_{-60}^{+80}	-129010_{-60}^{+50}	-17790_{-60}^{+70}	-119010_{-70}^{+60}	-5860 ± 50	-119080_{-70}^{+60}	-5890 ± 70	-119060 ± 70
D_{min} ⁽⁴⁾	$(2.84_{-0.04}^{+0.03}) \times 10^2$	$5.400_{-0.005}^{+0.004}$	$(2.84 \pm 0.02) \times 10^2$	$6.346_{-0.007}^{+0.006}$	$(2.62_{-0.04}^{+0.05}) \times 10^3$	$6.338_{-0.007}^{+0.006}$	$(2.59 \pm 0.06) \times 10^3$	6.340 ± 0.007
D_{max} ⁽⁵⁾	$(2.6_{-0.6}^{+1.0}) \times 10^5$	$(3_{-1}^{+2}) \times 10^4$	$(6_{-1}^{+2}) \times 10^4$	$1.54_{-0.07}^{+0.08}$	$(3_{-1}^{+2}) \times 10^4$	$1.53_{-0.07}^{+0.08}$	1.28 ± 0.06	$(8_{-7}^{+8}) \times 10^3$

(1) The ionized luminosity in unit of 10^{37} cm^{-1} . This value is automatically calculated by the `pion` model. The 10.6 keV component is looking at the unabsorbed SED, and the 7.1 keV component is looking at the absorbed SED (absorbed by the 10.6 keV component). (2) Column density in units of 10^{21} cm^{-2} . (3) Outflow velocity in units of km s^{-1} . (4) The lower limit on the position of the ionized wind. It was evaluated as $2GM_{\text{BH}}/v_{\text{out}}^2$ in units of R_{S} . (5) The upper limit on the position of the ionized wind. It was evaluated as $(L/\xi) \times N_{\text{H}}$ in units of R_{S} .

R. Blandford et al. 2019). The wind kinetic power to bolometric luminosity ratio are $\simeq 1.4C_{\text{v}}\%$ for the 7.1 keV absorption line and $\simeq 27C_{\text{v}}\%$ for the 10.6 keV absorption line. As discussed in the previous subsection, various possibilities of outflows are inferred from the emission lines; these absorbers might be a part of such outflow components, but with an extremely high velocity. In that case, a large covering factor (> 0.1) leads to detectable emission lines. However, there is no evidence of corresponding emission lines, implying $C_{\text{v}} < 0.1$. Thus, the wind from Cen A might not affect the feedback. On the other hand, the total power of the jet is estimated to be $P_{\text{jet}} = (1 - 2) \times 10^{43} \text{ erg s}^{-1}$, and an instantaneous jet power of $P_{\text{jet}} = 6.6 \times 10^{42} \text{ erg s}^{-1}$ (e.g. J. H. Croston et al. 2009; S. Wykes et al. 2013; S. G. Neff et al. 2015). The wind kinetic power is much lower than the jet power; therefore, the wind likely does not affect the jet collimation.

S. Yamada et al. (2024) reported a velocity gap at $\log v_{\text{out}} [\text{km s}^{-1}] \sim 4$. They suggested that the gap might be an observational bias, as absorption lines with velocities of $\log v_{\text{out}} [\text{km s}^{-1}] \sim 4$ would appear around the Fe-K edge and Fe-K β emission line, and thus could not be identified with the CCD resolution. In this observation, the 7.1 keV absorption line appeared precisely in the Fe-K edge structure, but XRISM/Resolve resolved the Fe-K edge and the absorption line. This demonstrates the excellent capability of XRISM/Resolve for line searches.

On the other hand, the 10.6 keV component has a very fast velocity ($\log v_{\text{out}} [\text{km s}^{-1}] = 5.11$). S. Yamada et al. (2024) compiled a list of AGNs that have UFOs with very fast outflow velocities ($\log v_{\text{out}} [\text{km s}^{-1}] \geq 5$). The list of AGNs with very fast outflow velocity in S. Yamada et al. (2024) is in Table 12. Most AGNs with outflow velocities above $\log v_{\text{out}} [\text{km s}^{-1}] \geq 5$ were quasars.

4.3. Relation with a large-scale outflow discovered by JWST

JWST/MIRI observations of the Cen A core detected the outflowing gas via ionized Ar II and Ne III lines.

They are narrow ($\sigma \sim 600 \text{ km s}^{-1}$) with velocity reaching approximately $+1000$ and -1400 km s^{-1} , respectively, within a $\sim 10^6 R_{\text{S}}$ (6 pc) region (A. Alonso-Herrero et al. 2025). They calculated the upper limit of the kinetic power to be $1.3 \times 10^{42} \text{ erg s}^{-1}$. If the distance of this outflow from the center is around 1 pc, it is similar to that estimated for the narrow collisionally ionized component. The kinetic power of the narrow ionized components observed by XRISM is also similar, suggesting the inner ionized outflow could drive the outer infrared outflow. A. Alonso-Herrero et al. (2025) suggested the infrared ionized outflow could be driven by a jet interacting with the interstellar medium rather than the outflow. Our results give the possibility that the AGN outflow could drive the infrared outflow.

5. CONCLUSIONS

In this study, we analyzed the broadband X-ray spectra (3–60 keV) of the nearby radio galaxy Centaurus A using joint XRISM/Resolve and NuSTAR observations. By performing a detailed spectral modeling with the SPEX code, we identified, for the first time, significant ionized emission components in the Fe-K band of Cen A. This marks a notable advancement in the study of circumnuclear environments in low-Eddington radio galaxies, where clear ionized features have rarely been reported.

The spectral modeling revealed three ionized emission components: one is broad and redshifted ($v_{\text{broad}} = 3100 \pm 500 \text{ km s}^{-1}$, $v_{\text{shift}} = 4000 \pm 500 \text{ km s}^{-1}$) and others are narrow redshifted and blueshifted ($v_{\text{broad}} = 400 \pm 100 \text{ km s}^{-1}$, $v_{\text{shift}} = 2600 \pm 100 \text{ km s}^{-1}$, and $v_{\text{broad}} = 550_{-80}^{+110} \text{ km s}^{-1}$, $v_{\text{shift}} = -1500 \pm 100 \text{ km s}^{-1}$), attributed to Fe XXV and Fe XXVI lines. The upper limit on the distance of the emitters is $1300 R_{\text{S}}$ or $8 \times 10^3 R_{\text{S}}$, assuming a photoionized plasma. The collisionally ionized plasma model can reproduce the narrow line components, and in that case, the distance could be as large as 0.5 pc, but within the torus. We cannot distinguish whether the velocity is due to inflow, outflow, or rotation.

In addition, absorption lines at 7.1 keV and 10.6 keV were detected, corresponding to Fe xxv absorption features. Modeling with the pion component suggests these are Fe xxv lines blueshifted due to UFOs with outflow velocities of $\sim 0.06c$ and $\sim 0.43c$, respectively. These absorption components are characterized by moderate ionization parameters ($\log \xi \sim 2.9 - 3.3$) and relatively low column densities ($N_{\text{H}} \sim 10^{21} \text{ cm}^{-2}$). These results demonstrate the high potential of XRISM/Resolve for characterizing AGN outflows and emission features in the Fe-K band. Our findings establish a new benchmark for the spectroscopic study of low-luminosity radio galaxies, contributing to a broader understanding of AGN unification.

Based on our discussion and considering the synergy with the outer infrared outflow discovered by JWST, the broad component is interpreted as an inner region inflow and/or outflow with a wide range of velocities, and the UFOs might be a part of this inner outflow traveling at an extremely high velocity. The narrow components would be outflowing shock-heated plasma pushed by past AGN activity at around 0.5 pc, which could in turn drive the outer infrared outflow.

ACKNOWLEDGMENTS

The authors thank the editors and the anonymous referee for their useful comments to improve the quality of this work. This paper employs a list of Chandra datasets, obtained by the Chandra X-ray Observatory, contained in the Chandra Data Collection DOI: [10.25574/cdc.514](https://doi.org/10.25574/cdc.514). A reproduction package is available at Zenodo DOI: [10.5281/zenodo.17908257](https://doi.org/10.5281/zenodo.17908257). This package includes data and scripts used to reproduce the fitting results and figures presented here. This work was supported by JSPS KAKENHI Grant Number JP25KJ1868 (TK), JP19K21884, JP20H01941, JP20H01947, JP20KK0071, JP23K20239, JP24K00672 (HN), JP23KJ0780 (TI), JP20H01946 (YU), JP21K13958 (MM), JP24KJ1507 (YN), JST SPRING Grant Number JPMJSP2132 (TK), NASA under award number 80GSFC24M0006 (TY), Canadian Space Agency grant 18XARMSTMA (LCG), Yamada Science Foundation (MM), and Tsinghua Dushi program (JM). We thank D. Rogantini, N. Kawakatsu, and M. Nomura for helpful discussions.

REFERENCES

- Akaike, H. 1974, *IEEE Transactions on Automatic Control*, 19, 716
- Alonso-Herrero, A., Hermosa Muñoz, L., Labiano, A., et al. 2025, arXiv e-prints, arXiv:2506.15286, doi: [10.48550/arXiv.2506.15286](https://doi.org/10.48550/arXiv.2506.15286)
- Awaki, H., Koyama, K., Inoue, H., & Halpern, J. P. 1991, *PASJ*, 43, 195, doi: [10.1093/pasj/43.2.195](https://doi.org/10.1093/pasj/43.2.195)
- Beckmann, V., Jean, P., Lubiński, P., Soldi, S., & Terrier, R. 2011, *A&A*, 531, A70, doi: [10.1051/0004-6361/201016020](https://doi.org/10.1051/0004-6361/201016020)
- Bianchi, S., Matt, G., Nicastro, F., Porquet, D., & Dubau, J. 2005, *MNRAS*, 357, 599, doi: [10.1111/j.1365-2966.2005.08661.x](https://doi.org/10.1111/j.1365-2966.2005.08661.x)
- Blandford, R., Meier, D., & Readhead, A. 2019, *ARA&A*, 57, 467, doi: [10.1146/annurev-astro-081817-051948](https://doi.org/10.1146/annurev-astro-081817-051948)
- Bogensberger, D., Miller, J., Kammoun, E., et al. 2024, *ApJ*, 961, 150, doi: [10.3847/1538-4357/ad1107](https://doi.org/10.3847/1538-4357/ad1107)
- Bogensberger, D., Nakatani, Y., Yaqoob, T., et al. 2025, *PASJ*, psaf084, doi: [10.1093/pasj/psaf084](https://doi.org/10.1093/pasj/psaf084)
- Boissay-Malaquin, R., Danehkar, A., Marshall, H. L., & Nowak, M. A. 2019, *ApJ*, 873, 29, doi: [10.3847/1538-4357/ab0082](https://doi.org/10.3847/1538-4357/ab0082)
- Borkar, A., Adhikari, T. P., Różańska, A., et al. 2021, *MNRAS*, 500, 3536, doi: [10.1093/mnras/staa3515](https://doi.org/10.1093/mnras/staa3515)
- Braito, V., Reeves, J. N., Matzeu, G. A., et al. 2018, *MNRAS*, 479, 3592, doi: [10.1093/mnras/sty1697](https://doi.org/10.1093/mnras/sty1697)
- Braito, V., Reeves, J. N., Severgnini, P., et al. 2021, *MNRAS*, 500, 291, doi: [10.1093/mnras/staa3264](https://doi.org/10.1093/mnras/staa3264)
- Braito, V., Reeves, J. N., Matzeu, G., et al. 2022, *ApJ*, 926, 219, doi: [10.3847/1538-4357/ac3763](https://doi.org/10.3847/1538-4357/ac3763)
- Buhariwalla, M. Z., Gallo, L. C., Mao, J., et al. 2024, *ApJ*, 971, 22, doi: [10.3847/1538-4357/ad4ee0](https://doi.org/10.3847/1538-4357/ad4ee0)
- Cappellari, M., Neumayer, N., Reunanen, J., et al. 2009, *MNRAS*, 394, 660, doi: [10.1111/j.1365-2966.2008.14377.x](https://doi.org/10.1111/j.1365-2966.2008.14377.x)
- Chakraborty, P., Ferland, G. J., Chatzikos, M., Guzmán, F., & Su, Y. 2021, *ApJ*, 912, 26, doi: [10.3847/1538-4357/abed4a](https://doi.org/10.3847/1538-4357/abed4a)
- Chartas, G., Brandt, W. N., & Gallagher, S. C. 2003, *ApJ*, 595, 85, doi: [10.1086/377299](https://doi.org/10.1086/377299)
- Chartas, G., Brandt, W. N., Gallagher, S. C., & Garmire, G. P. 2002, *ApJ*, 579, 169, doi: [10.1086/342744](https://doi.org/10.1086/342744)
- Chartas, G., Cappi, M., Hamann, F., et al. 2016, *ApJ*, 824, 53, doi: [10.3847/0004-637X/824/1/53](https://doi.org/10.3847/0004-637X/824/1/53)
- Chartas, G., Eracleous, M., Dai, X., Agol, E., & Gallagher, S. 2007, *ApJ*, 661, 678, doi: [10.1086/516816](https://doi.org/10.1086/516816)
- Chartas, G., Hamann, F., Eracleous, M., et al. 2014, *ApJ*, 783, 57, doi: [10.1088/0004-637X/783/1/57](https://doi.org/10.1088/0004-637X/783/1/57)

- Chartas, G., Saez, C., Brandt, W. N., Giustini, M., & Garmire, G. P. 2009, *ApJ*, 706, 644, doi: [10.1088/0004-637X/706/1/644](https://doi.org/10.1088/0004-637X/706/1/644)
- Chartas, G., Cappi, M., Vignali, C., et al. 2021, *ApJ*, 920, 24, doi: [10.3847/1538-4357/ac0ef2](https://doi.org/10.3847/1538-4357/ac0ef2)
- Crenshaw, D. M., & Kraemer, S. B. 2012, *ApJ*, 753, 75, doi: [10.1088/0004-637X/753/1/75](https://doi.org/10.1088/0004-637X/753/1/75)
- Crenshaw, D. M., Kraemer, S. B., & George, I. M. 2003, *ARA&A*, 41, 117, doi: [10.1146/annurev.astro.41.082801.100328](https://doi.org/10.1146/annurev.astro.41.082801.100328)
- Croston, J. H., Kraft, R. P., Hardcastle, M. J., et al. 2009, *MNRAS*, 395, 1999, doi: [10.1111/j.1365-2966.2009.14715.x](https://doi.org/10.1111/j.1365-2966.2009.14715.x)
- Di Gesu, L., Costantini, E., Piconcelli, E., et al. 2017, *A&A*, 608, A115, doi: [10.1051/0004-6361/201731853](https://doi.org/10.1051/0004-6361/201731853)
- Di Matteo, T., Springel, V., & Hernquist, L. 2005, *Nature*, 433, 604, doi: [10.1038/nature03335](https://doi.org/10.1038/nature03335)
- Fanaroff, B. L., & Riley, J. M. 1974, *MNRAS*, 167, 31P, doi: [10.1093/mnras/167.1.31P](https://doi.org/10.1093/mnras/167.1.31P)
- Faucher-Giguère, C.-A., & Quataert, E. 2012, *MNRAS*, 425, 605, doi: [10.1111/j.1365-2966.2012.21512.x](https://doi.org/10.1111/j.1365-2966.2012.21512.x)
- Foster, A., Chakraborty, P., Brickhouse, N., Smith, R., & Gall, A. 2025, in *American Astronomical Society Meeting Abstracts*, Vol. 246, 246th Meeting of the American Astronomical Society, 118.04
- Fruscione, A., McDowell, J. C., Allen, G. E., et al. 2006, in *SPIE*, Vol. 6270, *SPIE*, 62701V, doi: [10.1117/12.671760](https://doi.org/10.1117/12.671760)
- Fukazawa, Y., Furui, S., Hayashi, K., et al. 2016, *ApJ*, 821, 15, doi: [10.3847/0004-637X/821/1/15](https://doi.org/10.3847/0004-637X/821/1/15)
- Fukazawa, Y., Matake, H., Kayanoki, T., Inoue, Y., & Finke, J. 2022, *ApJ*, 931, 138, doi: [10.3847/1538-4357/ac6acb](https://doi.org/10.3847/1538-4357/ac6acb)
- Fukazawa, Y., Hiragi, K., Mizuno, M., et al. 2011, *ApJ*, 727, 19, doi: [10.1088/0004-637X/727/1/19](https://doi.org/10.1088/0004-637X/727/1/19)
- Fukumura, K., Tombesi, F., Kazanas, D., et al. 2014, *ApJ*, 780, 120, doi: [10.1088/0004-637X/780/2/120](https://doi.org/10.1088/0004-637X/780/2/120)
- Gallo, L. C., Miller, J. M., & Costantini, E. 2023, *arXiv e-prints*, arXiv:2302.10930, doi: [10.48550/arXiv.2302.10930](https://doi.org/10.48550/arXiv.2302.10930)
- Gandhi, P., Kawamuro, T., Díaz Trigo, M., et al. 2022, *Nature Astronomy*, 6, 1364, doi: [10.1038/s41550-022-01857-y](https://doi.org/10.1038/s41550-022-01857-y)
- Globus, N., & Levinson, A. 2016, *MNRAS*, 461, 2605, doi: [10.1093/mnras/stw1474](https://doi.org/10.1093/mnras/stw1474)
- Gofford, J., Reeves, J. N., McLaughlin, D. E., et al. 2015, *MNRAS*, 451, 4169, doi: [10.1093/mnras/stv1207](https://doi.org/10.1093/mnras/stv1207)
- Gofford, J., Reeves, J. N., Tombesi, F., et al. 2013, *MNRAS*, 430, 60, doi: [10.1093/mnras/sts481](https://doi.org/10.1093/mnras/sts481)
- Hagino, K., Done, C., Odaka, H., Watanabe, S., & Takahashi, T. 2017, *MNRAS*, 468, 1442, doi: [10.1093/mnras/stx559](https://doi.org/10.1093/mnras/stx559)
- Harris, G. L. H., Rejkuba, M., & Harris, W. E. 2010, *PASA*, 27, 457, doi: [10.1071/AS09061](https://doi.org/10.1071/AS09061)
- Harrison, F. A., Craig, W. W., Christensen, F. E., et al. 2013, *ApJ*, 770, 103, doi: [10.1088/0004-637X/770/2/103](https://doi.org/10.1088/0004-637X/770/2/103)
- HI4PI Collaboration, Ben Bekhti, N., Flöer, L., et al. 2016, *A&A*, 594, A116, doi: [10.1051/0004-6361/201629178](https://doi.org/10.1051/0004-6361/201629178)
- Ishisaki, Y., Kelley, R. L., Awaki, H., et al. 2025, *Journal of Astronomical Telescopes, Instruments, and Systems*, 11, 042023, doi: [10.1117/1.JATIS.11.4.042023](https://doi.org/10.1117/1.JATIS.11.4.042023)
- Iwata, T., Tanimoto, A., Odaka, H., et al. 2024, *PASJ*, 76, 923, doi: [10.1093/pasj/psae059](https://doi.org/10.1093/pasj/psae059)
- Kaastra, J. S. 2017, *A&A*, 605, A51, doi: [10.1051/0004-6361/201629319](https://doi.org/10.1051/0004-6361/201629319)
- Kaastra, J. S., & Bleeker, J. A. M. 2016, *A&A*, 587, A151, doi: [10.1051/0004-6361/201527395](https://doi.org/10.1051/0004-6361/201527395)
- Kaastra, J. S., Mewe, R., Liedahl, D. A., et al. 1996, *A&A*, 314, 547
- Kaastra, J. S., Raassen, A. J. J., de Plaa, J., & Gu, L. 2024, *SPEX X-ray spectral fitting package*, 3.08.00 Zenodo, doi: [10.5281/zenodo.10822753](https://doi.org/10.5281/zenodo.10822753)
- Kara, E., García, J. A., Lohfink, A., et al. 2017, *MNRAS*, 468, 3489, doi: [10.1093/mnras/stx792](https://doi.org/10.1093/mnras/stx792)
- Kayanoki, T., & Fukazawa, Y. 2022, *PASJ*, 74, 791, doi: [10.1093/pasj/psac036](https://doi.org/10.1093/pasj/psac036)
- Kelley, R. L., Awaki, H., Balleza, J. C., et al. 2025, *Journal of Astronomical Telescopes, Instruments, and Systems*, 11
- Koss, M. J., Ricci, C., Trakhtenbrot, B., et al. 2022, *ApJS*, 261, 2, doi: [10.3847/1538-4365/ac6c05](https://doi.org/10.3847/1538-4365/ac6c05)
- Laha, S., Reynolds, C. S., Reeves, J., et al. 2021, *Nature Astronomy*, 5, 13, doi: [10.1038/s41550-020-01255-2](https://doi.org/10.1038/s41550-020-01255-2)
- Lanzuisi, G., Giustini, M., Cappi, M., et al. 2012, *A&A*, 544, A2, doi: [10.1051/0004-6361/201219481](https://doi.org/10.1051/0004-6361/201219481)
- Li, C., Kaastra, J. S., Gu, L., et al. 2025, *A&A*, 694, A302, doi: [10.1051/0004-6361/202452911](https://doi.org/10.1051/0004-6361/202452911)
- Liddle, A. R. 2007, *MNRAS*, 377, L74, doi: [10.1111/j.1745-3933.2007.00306.x](https://doi.org/10.1111/j.1745-3933.2007.00306.x)
- Lobban, A. P., & Vaughan, S. 2014, *MNRAS*, 439, 1575, doi: [10.1093/mnras/stu002](https://doi.org/10.1093/mnras/stu002)
- Lodders, K., Palme, H., & Gail, H. P. 2009, *Landolt Börnstein*, 4B, 712, doi: [10.1007/978-3-540-88055-4_34](https://doi.org/10.1007/978-3-540-88055-4_34)
- Longinotti, A. L., Bianchi, S., Santos-Lleo, M., et al. 2007, *A&A*, 470, 73, doi: [10.1051/0004-6361:20066248](https://doi.org/10.1051/0004-6361:20066248)
- Luminari, A., Marinucci, A., Bianchi, S., et al. 2023, *ApJ*, 950, 160, doi: [10.3847/1538-4357/acd2d8](https://doi.org/10.3847/1538-4357/acd2d8)
- Mao, J., Kaastra, J. S., Mehdipour, M., et al. 2018, *A&A*, 612, A18, doi: [10.1051/0004-6361/201732162](https://doi.org/10.1051/0004-6361/201732162)

- Mao, J., Mehdipour, M., Kaastra, J. S., et al. 2019, *A&A*, 621, A99, doi: [10.1051/0004-6361/201833191](https://doi.org/10.1051/0004-6361/201833191)
- Matake, H., & Fukazawa, Y. 2023, *PASJ*, 75, 1124, doi: [10.1093/pasj/psad060](https://doi.org/10.1093/pasj/psad060)
- Matzeu, G. A., Braitto, V., Reeves, J. N., et al. 2019, *MNRAS*, 483, 2836, doi: [10.1093/mnras/sty3327](https://doi.org/10.1093/mnras/sty3327)
- Mehdipour, M., Kaastra, J. S., & Kallman, T. 2016, *A&A*, 596, A65, doi: [10.1051/0004-6361/201628721](https://doi.org/10.1051/0004-6361/201628721)
- Mehdipour, M., Kaastra, J. S., Eckart, M. E., et al. 2025, *A&A*, 699, A228, doi: [10.1051/0004-6361/202555623](https://doi.org/10.1051/0004-6361/202555623)
- Miller, J. M., Kaastra, J. S., Miller, M. C., et al. 2015, *Nature*, 526, 542, doi: [10.1038/nature15708](https://doi.org/10.1038/nature15708)
- Miller, J. M., Behar, E., Awaki, H., et al. 2025, *ApJL*, 985, L41, doi: [10.3847/2041-8213/add262](https://doi.org/10.3847/2041-8213/add262)
- Mizumoto, M., Ebisawa, K., Tsujimoto, M., et al. 2019a, *MNRAS*, 482, 5316, doi: [10.1093/mnras/sty3056](https://doi.org/10.1093/mnras/sty3056)
- Mizumoto, M., Izumi, T., & Kohno, K. 2019b, *ApJ*, 871, 156, doi: [10.3847/1538-4357/aaf814](https://doi.org/10.3847/1538-4357/aaf814)
- Murphy, K. D., & Yaqoob, T. 2009, *MNRAS*, 397, 1549, doi: [10.1111/j.1365-2966.2009.15025.x](https://doi.org/10.1111/j.1365-2966.2009.15025.x)
- Nakatani, Y., Ueda, Y., Ricci, C., et al. 2023, *MNRAS*, 523, 6239, doi: [10.1093/mnras/stad1836](https://doi.org/10.1093/mnras/stad1836)
- Neff, S. G., Eilek, J. A., & Owen, F. N. 2015, *ApJ*, 802, 87, doi: [10.1088/0004-637X/802/2/87](https://doi.org/10.1088/0004-637X/802/2/87)
- Neumayer, N., Cappellari, M., Reunanen, J., et al. 2007, *ApJ*, 671, 1329, doi: [10.1086/523039](https://doi.org/10.1086/523039)
- Noda, H., Yamada, S., Ogawa, S., et al. 2025, *arXiv e-prints*, arXiv:2510.18027, doi: [10.48550/arXiv.2510.18027](https://doi.org/10.48550/arXiv.2510.18027)
- Nomura, M., & Ohsuga, K. 2017, *MNRAS*, 465, 2873, doi: [10.1093/mnras/stw2877](https://doi.org/10.1093/mnras/stw2877)
- Page, M. J., Soria, R., Zane, S., Wu, K., & Starling, R. L. C. 2004, *A&A*, 422, 77, doi: [10.1051/0004-6361:20034451](https://doi.org/10.1051/0004-6361:20034451)
- Pinto, C., Kaastra, J. S., Costantini, E., & Verbunt, F. 2010, *A&A*, 521, A79, doi: [10.1051/0004-6361/201014836](https://doi.org/10.1051/0004-6361/201014836)
- Porquet, D., Dubau, J., & Grosso, N. 2010, *SSRv*, 157, 103, doi: [10.1007/s11214-010-9731-2](https://doi.org/10.1007/s11214-010-9731-2)
- Pounds, K. A., Nandra, K., Stewart, G. C., & Leighly, K. 1989, *MNRAS*, 240, 769, doi: [10.1093/mnras/240.4.769](https://doi.org/10.1093/mnras/240.4.769)
- Proga, D., & Kallman, T. R. 2004, *ApJ*, 616, 688, doi: [10.1086/425117](https://doi.org/10.1086/425117)
- Psaradaki, I., Costantini, E., Rogantini, D., et al. 2023, *A&A*, 670, A30, doi: [10.1051/0004-6361/202244110](https://doi.org/10.1051/0004-6361/202244110)
- Quataert, E., & Narayan, R. 1999, *ApJ*, 520, 298, doi: [10.1086/307439](https://doi.org/10.1086/307439)
- Reeves, J. N., Braitto, V., Chartas, G., et al. 2020, *ApJ*, 895, 37, doi: [10.3847/1538-4357/ab8cc4](https://doi.org/10.3847/1538-4357/ab8cc4)
- Reeves, J. N., Braitto, V., Nardini, E., et al. 2018, *ApJL*, 854, L8, doi: [10.3847/2041-8213/aaae1](https://doi.org/10.3847/2041-8213/aaae1)
- Reeves, J. N., Pounds, K., Uttley, P., et al. 2005, *ApJL*, 633, L81, doi: [10.1086/498568](https://doi.org/10.1086/498568)
- Ricci, C., & Paltani, S. 2023, *ApJ*, 945, 55, doi: [10.3847/1538-4357/acb5a6](https://doi.org/10.3847/1538-4357/acb5a6)
- Ricci, C., Ho, L. C., Fabian, A. C., et al. 2018, *MNRAS*, 480, 1819, doi: [10.1093/mnras/sty1879](https://doi.org/10.1093/mnras/sty1879)
- Rogantini, D., Costantini, E., Zeegers, S. T., et al. 2018, *A&A*, 609, A22, doi: [10.1051/0004-6361/201731664](https://doi.org/10.1051/0004-6361/201731664)
- Saez, C., & Chartas, G. 2011, *ApJ*, 737, 91, doi: [10.1088/0004-637X/737/2/91](https://doi.org/10.1088/0004-637X/737/2/91)
- Shi, F., Li, Z., Yuan, F., & Zhu, B. 2021, *Nature Astronomy*, 5, 928, doi: [10.1038/s41550-021-01394-0](https://doi.org/10.1038/s41550-021-01394-0)
- Shi, F., Yuan, F., Tombesi, F., & Xie, F.-g. 2025, *ApJ*, 985, 88, doi: [10.3847/1538-4357/adcc17](https://doi.org/10.3847/1538-4357/adcc17)
- Shu, X. W., Yaqoob, T., & Wang, J. X. 2010, *ApJS*, 187, 581, doi: [10.1088/0067-0049/187/2/581](https://doi.org/10.1088/0067-0049/187/2/581)
- Sim, S. A., Proga, D., Miller, L., Long, K. S., & Turner, T. J. 2010, *MNRAS*, 408, 1396, doi: [10.1111/j.1365-2966.2010.17215.x](https://doi.org/10.1111/j.1365-2966.2010.17215.x)
- Speith, R., Riffert, H., & Ruder, H. 1995, *Computer Physics Communications*, 88, 109, doi: [10.1016/0010-4655\(95\)00067-P](https://doi.org/10.1016/0010-4655(95)00067-P)
- Sugiura, N. 1978 *Communications in Statistics—Theory and Methods A*, 7, 13, doi: [10.1080/03610927808827599](https://doi.org/10.1080/03610927808827599)
- Tan, M. Y. J., & Biswas, R. 2012, *MNRAS*, 419, 3292, doi: [10.1111/j.1365-2966.2011.19969.x](https://doi.org/10.1111/j.1365-2966.2011.19969.x)
- Tarter, C. B., Tucker, W. H., & Salpeter, E. E. 1969, *ApJ*, 156, 943, doi: [10.1086/150026](https://doi.org/10.1086/150026)
- Tashiro, M., Kelley, R., Watanabe, S., et al. 2025, *PASJ*, 77, S1, doi: [10.1093/pasj/psaf023](https://doi.org/10.1093/pasj/psaf023)
- Tomaru, R., Done, C., & Mao, J. 2023, *MNRAS*, 518, 1789, doi: [10.1093/mnras/stac3210](https://doi.org/10.1093/mnras/stac3210)
- Tombesi, F., Cappi, M., Reeves, J. N., et al. 2013, *MNRAS*, 430, 1102, doi: [10.1093/mnras/sts692](https://doi.org/10.1093/mnras/sts692)
- Tombesi, F., Cappi, M., Reeves, J. N., et al. 2011, *ApJ*, 742, 44, doi: [10.1088/0004-637X/742/1/44](https://doi.org/10.1088/0004-637X/742/1/44)
- Tombesi, F., Sambruna, R. M., Reeves, J. N., et al. 2010, *ApJ*, 719, 700, doi: [10.1088/0004-637X/719/1/700](https://doi.org/10.1088/0004-637X/719/1/700)
- Tombesi, F., Tazaki, F., Mushotzky, R. F., et al. 2014, *MNRAS*, 443, 2154, doi: [10.1093/mnras/stu1297](https://doi.org/10.1093/mnras/stu1297)
- Tombesi, F., Veilleux, S., Meléndez, M., et al. 2017, *ApJ*, 850, 151, doi: [10.3847/1538-4357/aa9579](https://doi.org/10.3847/1538-4357/aa9579)
- Urry, C. M., & Padovani, P. 1995, *PASP*, 107, 803, doi: [10.1086/133630](https://doi.org/10.1086/133630)
- Vasudevan, R. V., & Fabian, A. C. 2007, *MNRAS*, 381, 1235, doi: [10.1111/j.1365-2966.2007.12328.x](https://doi.org/10.1111/j.1365-2966.2007.12328.x)
- Walton, D. J., Nardini, E., Gallo, L. C., et al. 2019, *MNRAS*, 484, 2544, doi: [10.1093/mnras/stz115](https://doi.org/10.1093/mnras/stz115)
- Wang, J. X., Wang, T. G., Tozzi, P., et al. 2005, *ApJL*, 631, L33, doi: [10.1086/496970](https://doi.org/10.1086/496970)

- Wojdowski, P. S., Liedahl, D. A., Sako, M., Kahn, S. M., & Paerels, F. 2003, *ApJ*, 582, 959, doi: [10.1086/344821](https://doi.org/10.1086/344821)
- Wykes, S., Croston, J. H., Hardcastle, M. J., et al. 2013, *A&A*, 558, A19, doi: [10.1051/0004-6361/201321622](https://doi.org/10.1051/0004-6361/201321622)
- XRISM Collaboration, Audard, M., Awaki, H., et al. 2024, *ApJL*, 973, L25, doi: [10.3847/2041-8213/ad7397](https://doi.org/10.3847/2041-8213/ad7397)
- Xrism Collaboration, Audard, M., Awaki, H., et al. 2025, *Nature*, 641, 1132, doi: [10.1038/s41586-025-08968-2](https://doi.org/10.1038/s41586-025-08968-2)
- Yamada, S., Kawamuro, T., Mizumoto, M., et al. 2024, *ApJS*, 274, 8, doi: [10.3847/1538-4365/ad5961](https://doi.org/10.3847/1538-4365/ad5961)
- Yaqoob, T. 2024, *MNRAS*, 527, 1093, doi: [10.1093/mnras/stad3257](https://doi.org/10.1093/mnras/stad3257)
- Yaqoob, T., George, I. M., Kallman, T. R., et al. 2003, *ApJ*, 596, 85, doi: [10.1086/377687](https://doi.org/10.1086/377687)
- Yaqoob, T., & Padmanabhan, U. 2004, *ApJ*, 604, 63, doi: [10.1086/381731](https://doi.org/10.1086/381731)
- Zheng, Z. Y., & Wang, J. X. 2008, *ApJ*, 688, 116, doi: [10.1086/592141](https://doi.org/10.1086/592141)
- Zhou, H., Shi, X., Yuan, W., et al. 2019, *Nature*, 573, 83, doi: [10.1038/s41586-019-1510-y](https://doi.org/10.1038/s41586-019-1510-y)

APPENDIX

A. ABSORPTION LINE VERIFICATION

Whether the absorption lines are real is an important question and should be investigated to determine whether they are not pixel-independent, time-independent, or count-rate dependent. We verified the 7.1 keV and 10.6 keV absorption lines. We split the Resolve data by region, time frame, and flux level to verify the pixel dependence, time dependence, and flux dependence. When divided by time, various flux levels are included, and when divided by flux level, various observation times are included. The total count is 4.71×10^5 counts.

A.1. Region

First, we split the Resolve data into the regions (Fig. 8). Each region contains 16 pixels. The counts for each region are listed in Table 11. From the region split spectra (Fig. 9), the Fe-K β emission line and the 10.6 keV absorption line are visible. The 7.1 keV is not easily seen, although an absorption line structure is required compared to the Fe-K edge.

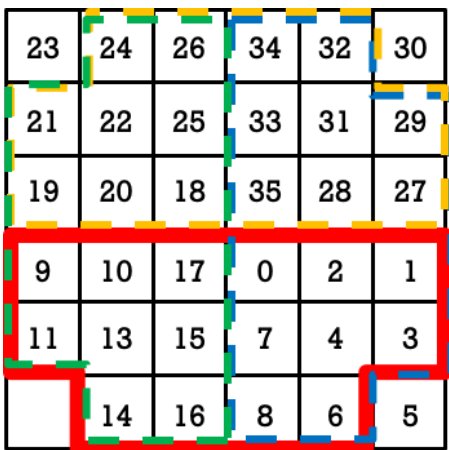


Figure 8. The XRISM/Resolve data was split into 16 pixels each for red, blue, yellow, and green regions. Referred from The XRISM Proposers’ Observatory Guide ^a (Fig. 5.1).

^a<https://heasarc.gsfc.nasa.gov/docs/xrism/proposals/POG/Resolve.html>

Table 11. Counts for each region

Region	Counts	Ratio
Bottom (red)	2.32×10^5	0.49
Right (blue)	2.21×10^5	0.47
Top (yellow)	2.11×10^5	0.45
Left (green)	2.22×10^5	0.47
Average	2.22×10^5	0.47

A.2. Time frame

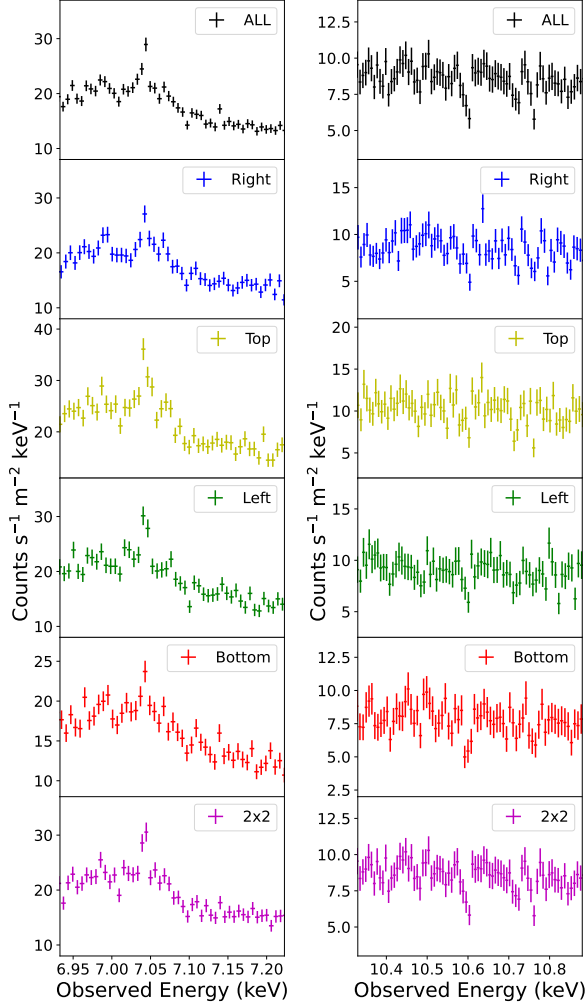
The average count of the region split corresponds to 106.054 ksec. Therefore, we subtracted the data into the three timeframes to 106.054 ksec. The first 106 ksec subtracted was Timeframe 1 (TF1), the middle was Timeframe 2 (TF2), and the last was Timeframe 3 (TF3). The line clarity from the time split spectra (Fig. 10) is similar to the region split spectrum, with the Fe-K β emission line and 10.6 keV absorption lines seen. However, the 7.1 keV absorption line is difficult to see.

A.3. Flux level

We subtracted the data into the three flux levels (corresponding to 106.054 ksec) as a timeframe. The data were sorted by count order and split into flux levels. Flux level 1 is a higher rate (> 1.98 cts), Flux level 2 is a medium count rate (1.30–2.06 cts), and Flux level 3 is the lower rate (< 1.98 cts). From the flux split spectra (Fig. 11), the line clarity is similar to the region split spectrum, with the Fe-K β emission line and 10.6 keV absorption lines seen. However, the 7.1 keV absorption line is difficult to see.

A.4. Simulation

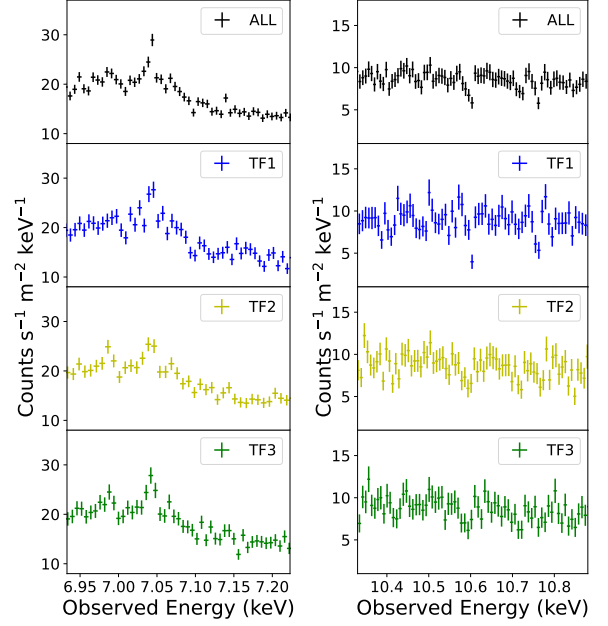
To investigate the significance of the 10.6 keV absorption line, we simulated the Resolve spectrum. For the 10.6 keV absorption line, we fitted the 10.2 – 11.2 keV Resolve spectra with a power-law and line model (Gaussian) and obtained the *EW* of the line ($EW = 5.5$ eV). We simulated two cases (1,000 times for each case): the Resolve spectra, with and without (Fig. 12 & 13) an absorption line. The exposure time was set to 106.054 ksec as a subset of the Time frame and flux level. In addition, we fitted all the Region split spectra, the Flux split spectra, and the Time split spectra with a power-law and line model (Gaussian) and obtained the *EW*



(a) 6.8 – 7.4 keV band (b) 10.4 – 10.95 keV band

Figure 9. Region split Resolve spectra, wherein the black point, blue point, yellow point, green point, red point, and magenta point represent the total pixel, right region, top region, left region, bottom region, and central 2×2 pixel region spectrum, respectively. The spectrum is binned by a factor of 2 after the optimal binning for visual clarity.

of the line (Fig. 13). The histogram was fitted with a Gaussian; the EW center is 5.17 eV, and σ is 2.5 eV. The all case (The region, time, flux split spectra) is in the 1σ . In the Fig. 12 we assumed there is no absorption line in 10.2 – 11.2 keV. We simulated the Resolve spectrum without the absorption line and fitted it with the line model. The histogram was fitted with a Gaussian; the EW center is 1.52 eV, and σ is 1.8 eV. Therefore, the 10.6 keV absorption line ($EW = 5.5$ eV) is a 98.6% level.



(a) 6.8 – 7.4 keV band (b) 10.4 – 10.95 keV band

Figure 10. Time split Resolve spectra, wherein the black, blue, yellow, and green points represent the total time, timeframe 1, timeframe 2, and timeframe three spectra, respectively. The spectrum is binned by a factor of 2 after the optimal binning for visual clarity.

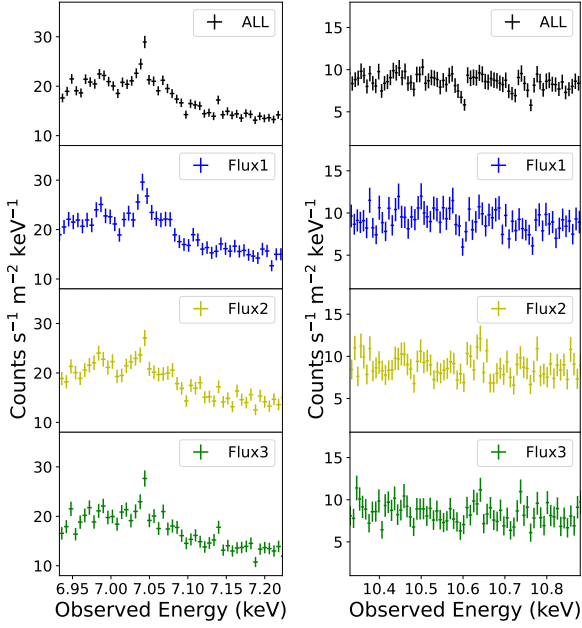
B. DIFFERENCES BETWEEN H-LIKE AND HE-LIKE MODEL CURVES IN PHOTO-IONIZATION ABSORPTION

C. UFOS WITH VERY FAST OUTFLOW VELOCITY

Table 12. The list of the UFOs with very fast outflow velocity ($\log v_{\text{out}} [\text{km s}^{-1}] \geq 5$) in *S. Yamada et al. (2024)*.

Object	Ra., Dec.	Redshift	Type	$\log v_{\text{out}}$	Reference
CXOCDFS J033260.0–274748	03h32m60.0s, –27d47m48s	2.579	QSO	5.40	[1, 2]
H 1413+117	14h15m46.2s, +11d29m44s	2.560	QSO	5.30	[3]
APM 08279+5255	08h31m41.7s, +52d45m18s	3.910	QSO	5.02 – 5.25	[4-10]
HS 1700+6416	17h01m00.6s, +64d12m09s	2.735	QSO	5.06 – 5.24	[10, 11]
SDSS J1029+2623	10h29m11.9s, +26d23m38s	2.197	QSO	5.24	[10]
SDSS J1128+2402	11h28m18.5, +24d02m18s	1.608	QSO	5.24	[10]
SDSS J0921+2854	09h21m15.5s, +28d54m44s	1.410	QSO	5.09 – 5.20	[10]
NGC 4151	12h10m32.6s, +39d24m21s	0.0033	1.5	5.24	[12]
PDS 456	17h28m19.8s, –14d15m56s	0.1840	1/QSO	5.03 – 5.16	[13-15]
SDSS J1442+4055	14h42m54.8s, +40d55m36s	2.593	QSO	5.15	[10]
PKS 1549–79	15h56m58.9s, –79d14m04s	0.1522	NLS1	5.11	[16]
HS 0810+2554	08h13m31.3s, +25d45m03s	1.51	QSO	5.09 – 5.11	[10, 17-18]
Mrk 231	12h56m14.2s, +56d52m25s	0.0422	1.0	5.10	[19]
PG 1211+143	12h14m17.7s, +14d03m13s	0.0809	NLS1	5.10	[20]
NGC 2992	09h45m42.1, –14d19m35s	0.0077	1.9	5.02 – 5.09	[21]
IRAS 00521–7054	00h53m56.2s, –70d38m04s	0.0689	2.0	5.08	[22]
PG 1115+080	11h18m16.9s, +07d45m59s	1.733	QSO	5.05	[3, 10, 23]
Ark 564	22h42m39.3s, +29d43m31s	0.0240	NLS1	5.03	[24]
MCG-03-58-007	22h49m37.1s, –19d16m26	0.0323	2.0	5.01 – 5.03	[25-28]
SDSS J1353+1138	13h53m06.3s, +11d38m05s	1.627	QSO	5.01	[10]

$\log v_{\text{out}}$: Logarithm of the outflow velocity in unit km s^{-1} . References; (1) *J. X. Wang et al. (2005)*, (2) *Z. Y. Zheng & J. X. Wang (2008)*, (3) *G. Chartas et al. (2007)*, (4) *G. Chartas et al. (2002)*, (5) *G. Chartas et al. (2009)*, (6) *C. Saez & G. Chartas (2011)*, (7) *J. Gofford et al. (2013)*, (8) *J. Gofford et al. (2015)*, (9) *K. Hagino et al. (2017)*, (10) *G. Chartas et al. (2021)*, (11) *G. Lanzuisi et al. (2012)*, (12) *H. Zhou et al. (2019)*, (13) *J. N. Reeves et al. (2018)*, (14) *R. Boissay-Malaquin et al. (2019)*, (15) *J. N. Reeves et al. (2020)*, (16) *F. Tombesi et al. (2014)*, (17) *G. Chartas et al. (2014)*, (18) *G. Chartas et al. (2016)*, (19) *M. Mizumoto et al. (2019b)*, (20) *J. N. Reeves et al. (2005)*, (21) *A. Luminari et al. (2023)*, (22) *D. J. Walton et al. (2019)*, (23) *G. Chartas et al. (2003)*, (24) *E. Kara et al. (2017)*, (25) *V. Braitto et al. (2018)*, (26) *G. A. Matzeu et al. (2019)*, (27) *V. Braitto et al. (2021)*, (28) *V. Braitto et al. (2022)*



(a) 6.8 – 7.4 keV band (b) 10.4 – 10.95 keV band

Figure 11. Flux split Resolve spectra, wherein the black, blue, yellow, and green points represent the time, flux level 1, flux level 2, and flux level 3 spectra, respectively. The spectrum is binned by a factor of 2 after the optimal binning for visual clarity.

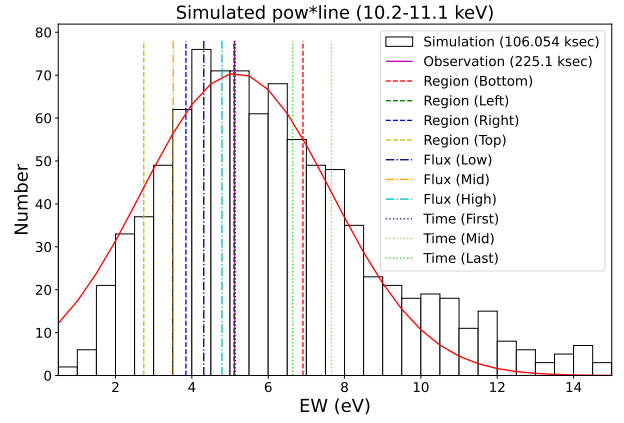
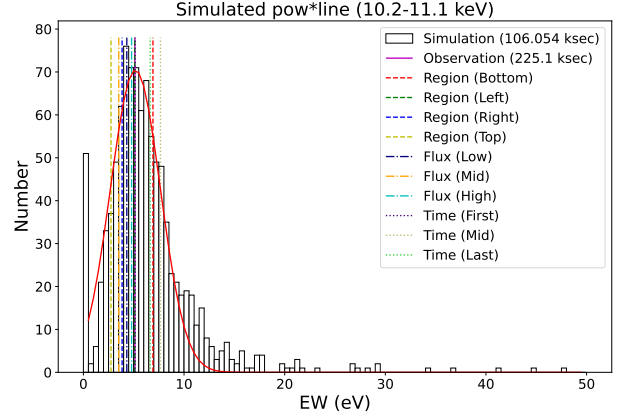


Figure 13. A Histogram of the EW. Simulated the 10.2–11.2 keV Resolve spectrum and fitted with a power law and a line model (Gaussian). A histogram was fitted with a Gaussian (red line, EW center is 5.17 eV, σ is 2.5 eV).

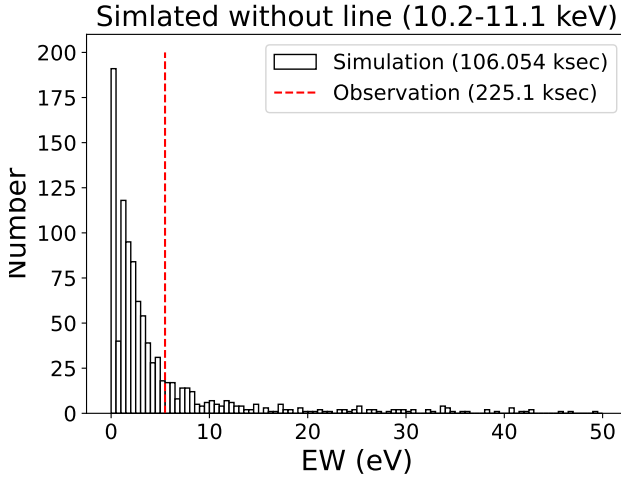


Figure 12. A Histogram of the EW. Simulated the 10.2 – 11.2 keV Resolve spectrum and fitted with a power law (without the line).

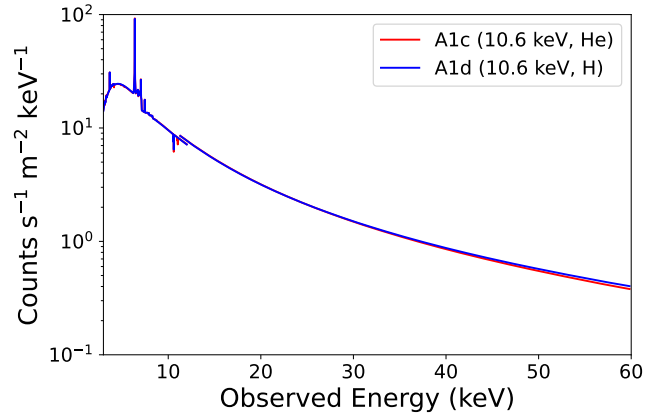


Figure 14. Differences between H-like and He-like model curves in photo-ionization absorption. The red line and the blue line represent the He-like Fe case and the H-like Fe case, respectively.